Redox Biology 43 (2021) 102006

Contents lists available at ScienceDirect

Redox Biology

journal homepage: www.elsevier.com/locate/redox

Tumor resistance to ferroptosis driven by Stearoyl-CoA Desaturase-1 (SCD1) in cancer cells and Fatty Acid Biding Protein-4 (FABP4) in tumor microenvironment promote tumor recurrence

Géraldine Luis [a,b,1], Adrien Godfroid [a,b,1], Shin Nishiumi [c,g], Jonathan Cimino [a,d,j], Silvia Blacher [a], Erik Maquoi [a], Coline Wery [a,b], Alice Collignon [a,b], Rémi Longuespée [d,e], Laetitia Montero-Ruiz [a,b], Isabelle Dassoul [a], Naima Maloujahmoum [f], Charles Pottier [a,b], Gabriel Mazzucchelli [d], Edwin Depauw [d], Akeila Bellahcène [f], Masaru Yoshida [c,h,i], Agnès Noel [a], Nor Eddine Sounni [a,b,*]

[a] Laboratory of Biology of Tumor and Developmental Biology, GIGA Cancer, Liège University, Liège, Belgium
[b] Cancer Metabolism and Tumor Microenvironment Group, GIGA Cancer, Liège University, Liège, Belgium
[c] Division of Gastroenterology, Department of Internal Medicine, Kobe University Graduate School of Medicine, Kobe, Japan
[d] Mass Spectrometry Laboratory, MolSys Research Unit, University of Liège, Liège, Belgium
[e] Department of Clinical Pharmacology and Pharmacoepidemiology, Heidelberg University Hospital, Heidelberg, Germany
[f] Metastasis Research Laboratory, GIGA Cancer, University of Liège, 4000, Liège, Belgium
[g] Department of Omics Medicine, Hyogo College of Medicine, Nishinomiya, Japan
[h] Division of Metabolomics Research, Department of Internal Related, Kobe University Graduate School of Medicine, Kobe, Japan
[i] AMED-CREST, AMED, Kobe, Japan
[j] Clinical Research Unit, Fondation Hôpitaux Robert Schuman, Hôpitaux Robert Schuman, Luxembourg

ARTICLE INFO

Keywords:
Lipid metabolism
Hypoxia
Reoxygenation
Drug-resistance
Tumor-microenvironment
ROS-ferroptosis

ABSTRACT

Problem: Tumor recurrence is a major clinical issue that represents the principal cause of cancer-related deaths, with few targetable common pathways. Mechanisms by which residual tumors persist and progress under a continuous shift between hypoxia-reoxygenation after neoadjuvent-therapy are unknown. In this study, we investigated the role of lipid metabolism and tumor redox balance in tumor recurrence.
Methods: Lipidomics, proteomics and mass spectrometry imaging approaches where applied to mouse tumor models of recurrence. Genetic and pharmacological inhibitions of lipid mediators in tumors were used in vivo and in functional assays in vitro.
Results: We found that stearoyl-CoA desaturase-1 (SCD1) expressed by cancer cells and fatty acid binding protein-4 (FABP4) produced by tumor endothelial cells (TECs) and adipocytes in the tumor microenvironment (TME) are essential for tumor relapse in response to tyrosine kinase inhibitors (TKI) and chemotherapy. SCD1 and FABP4 were also found upregulated in recurrent human breast cancer samples and correlated with worse prognosis of cancer patients with different types of tumors. Mechanistically, SCD1 leads to fatty acid (FA) desaturation and FABP4 derived from TEM enhances lipid droplet (LD) in cancer cells, which cooperatively protect from oxidative stress-induced ferroptosis. We revealed that lipid mobilization and desaturation elicit tumor intrinsic antioxidant and anti-ferroptotic resources for survival and regrowth in a harsh TME. Inhibition of lipid transport from TME by FABP4 inhibitor reduced tumor regrowth and by genetic — or by pharmacological — targeting SCD1 in vivo, tumor regrowth was abolished completely.
Conclusion: This finding unveils that it is worth taking advantage of tumor lipid addiction, as a tumor vulnerability to design novel treatment strategy to prevent cancer recurrence.

---

[*] Corresponding author. Cancer Metabolism and Tumor Microenvironment Group, Laboratory of Tumor and Developmental Biology, GIGA-cancer, Liège University, Liège, Belgium.

E-mail addresses: geraldine.luis@chuliege.be (G. Luis), adrien.godfroid@outlook.be (A. Godfroid), nesounni@uliege.be (N.E. Sounni).

[1] These authors contributed equally.

https://doi.org/10.1016/j.redox.2021.102006
Received 9 April 2021; Received in revised form 4 May 2021; Accepted 10 May 2021
Available online 14 May 2021
2213-2317/© 2021 The Authors. Published by Elsevier B.V. This is an open access article under the CC BY-NC-ND license (http://creativecommons.org/licenses/by-nc-nd/4.0/).

1. Introduction

Systemic therapies have improved overall survival for many cancers, but cancer recurrence is the most shared problem of many primary treatment modalities for cancer [1]. How short and long-term tumor resurgences occur after treatment cessation, and how cancer cell adapt to the generated hypoxic and metabolic stresses is yet to be understood. Unlike normal tissue, cancer cells evolve under metabolic and oxidative stress conditions, which are favorable or unfavorable to their growth depending on their moderate or excessive levels respectively, and on the tumor intrinsic anti-oxidant and stress defenses [2–5]. Fluctuations in oxygen and nutrient disposal under an hypoxic tumor microenvironment (TME) can restrict tumor growth, but can also alter cancer phenotype and conversion to more malignant tumors [6]. Small residual tumors left after chemotherapies or targeted therapies may persist under a continuous shift between hypoxia-reoxygenation in TME during treatments, and evolve later into relapse and aggressive tumors [7]. Naturally occurring or treatment-exacerbated hypoxia and reoxygenation lead to persistent elevated oxidative stress in tumors that can alter the redox power of cancer cells [8]. Altered redox balance and redox signaling are implicated in genomic instability, tumor metabolism reprogramming [8,9], malignant progression and resistance to treatment [10,11]. Redox equilibrium depends on the intricate interplay between free radical producing reactions and scavenging factor systems such as superoxide dismutases (SODs), catalase, glutathione peroxidase (GPX), glutathione reductase (GR), peroxiredoxin and thioredoxin [11–13]. Abnormal accumulation of reactive oxygen species (ROS) leading to peroxidation (-OOH) of polyunsaturated fatty acids (PUFAs) can trigger ferroptosis, an iron-dependent non-apoptotic cell death [14–16], which might play an important role in tumor sensitization to anticancer drugs. Cancer cell escape from ferroptosis has been reported as key element in resistance to drugs [17], which paved the way for investigations on ferroptosis inducers as potential new anti-cancer drugs. Yet, the upstream intricate balance between ROS and lipids that determines molecular-pathway driving relapse in ferroptosis resistant cancers remains unknown.

The emergence of metabolic adaptation in resistance to therapeutics has paved the way to the exploration of targeting metabolic vulnerabilities of cancer cells to overcome drug resistance [18–20]. We and others have reported that *de novo* fatty acid synthesis is an emerging key driver of cancer malignancy dependent on the hypoxic and metabolic stress induced by antiangiogenic treatment [19,21]. Several studies have documented the key contribution of lipid metabolism during cancer adaptation to acidosis [22] and of lipid addiction during cancer progression [19–23]. Here, we uncovered a specific role of lipid desaturation and transport in tumor adaptation to oxidative stress caused by hypoxia-reoxygenation exacerbated by TKI or cisplatin treatment and discontinuation. We show that lipid desaturation by SCD1 in cancer cells and lipid transport by FABP4 produced by tumor endothelial cells (TECs) promote cancer cell survival and resistance to ferroptosis in TME. Blocking FABP4 and SCD1 activities in tumors inhibited these processes and drastically reduced tumor recurrence. Our results offer the opportunity to use a novel vulnerability to block cancer progression and recurrence after treatment.

2. Materials and methods

2.1. Cell lines

Human breast cancer (MDA-MB-231) and mouse Lewis Lung Carcinoma (LLC) were purchased from American Type Culture Collection (ATCC) (Manassas, USA). Human Umbilical Vein Endothelial Cells (HUVEC) were purchased from Lonza. Cell line authentication for interspecies contamination, was performed by Leibniz-Institute DSMZ (GmbH, Braunschweig, Germany). Cell lines were tested by MycoALert Kit 139 (Lonza) to ensure that they were Mycoplasma-free before in vitro and in vivo experiments. Cancer cells were grown in Dulbecco's modified Eagles's medium (DMEM) and HUVECs were cultured in EBM-2 basal medium (Lonza, CC-3156) and EGM-2 SingleQuots supplements (Lonza, CC-4176). Culture medium was supplemented with 10% fetal bovine serum (FBS), L-glutamine (2 mM), penicillin (100 U/ml), and streptomycin (100 μg/ml) except EBM medium which was supplemented with 2% FBS.

2.2. Human samples

Human primary breast cancer samples (n = 23) and their corresponding metastatic relapses (n = 22) were provided by the Biobank of the University Hospital of Liege (Liege University, Belgium). Human sample collection for research was conducted in accordance with the recognized ethical guideline of Declaration of Helsinki and approved by the institutional Ethics Committee of the University Hospital of Liege (Liege, Belgium; file #B707201111974).

2.3. Mouse models

In vivo tumor growth and regrowth (relapse) after TKIs (sunitinib or sorafenib) treatment cessation [19] and the effect of inhibitors of SCD1 (SCD1 Inh) or FABP4 (FABP4 Inh) Inh were evaluated on MDA-M231 xenografts grown in immunodeficient RAG1−/− mice (6–8 weeks old) (The Jackson Laboratory) or syngeneic LLC tumor grown in C57bl/6 (6–8 weeks old) mice (Charles River). For the assays using SCD1 Inhibitor (SCD1 Inh) or FABP4 Inhibitor (FABP4 Inh), mice bearing MDA-MB231 tumors (50–70 mm^3) or LLC tumors (50–100 mm^3) were administered with the vehicle, SCD1 Inh (40 mg/kg/day) or FABP4 Inh (40 mg/kg/day), in combination with TKI or by a sequential treatment at re-oxygenation phase. SCD1 Inh and FABP4 Inh were administered in mice for 30 days (for RAG−/−) or 14 days (for C57bl/c) in combination with TKI or during TKI-withdrawal by gavage. For treatment with RSL3 (20 mg/kg), drug was administered in mice bearing LLC tumors by i.p. injection every other day for 2 weeks. For cisplatin, BALB/c mice bearing 4T1 tumors (50–100 mm^3) were administered by i.p. injection of vehicle (0.7% DMSO in PBS) or cisplatin (7 mg/kg/week) for 3 weeks. All animal procedures were performed according to the Federation of European Laboratory Animal Sciences Associations (FELASA) within the accredited institutional animal facility and the approved animal protocols #1990 and #1990 at Liège University, Belgium.

2.4. Drug preparation and administration in mice

TKIs, sunitinib malate/SU11248/SUTENT and sorafenib/Nexavar were purchased from LC Laboratories (Woburn, MA) and prepared as described previously in Ref. [19].

Briefly, sunitinib (4 mg/ml) was suspended in vehicle consisting of 0.5% carboxymethylcellulose (CMC), 1.8% NaCl, 0.4% Tween-80, 0.9% benzyl alcohol and ultrapure water. Sorafenib (5 mg/ml) was suspended in Kremofor, ethanol 95%, H2O 1/1/6. Mice bearing tumors were treated with TKIs (sunitinib: 40 mg/kg/day or sorafenib: 20 mg/kg/day) for 30 days for MDA-MB231 xenografts and 15 days for LLC tumors followed by the drug washout period (re-oxygenation phase) that was 3 and 2 weeks for the MDA-MB23 and LLC tumors, respectively. For in vitro experiments, SCD1 Inh (Abcam, ab142089) was dissolved in DMSO at 100 mM and stored at −20. For in vivo studies, SCD1 Inh (DC Chemicals DC5893) [24] was dissolved in DMSO (vehicle) at 80 mg/ml as stock solution and diluted 10X in PBS before administration in mice. Mice bearing MDA-MB231 or LLC tumors were treated by gavage with vehicle (0.1 % DMSO in sterile PBS) or with SCD1 Inh (40 mg/kg/day) alone, in combination with TKI or after treatment cessation for the indicated periods. For the use of FABP4 Inh in vitro, FABP4 Inh (Bidepharmatech, BD62694) [25] was dissolved in DMSO at 25 mM stock solution and used at indicated doses. For in vivo studies, FABP4 Inh was prepared in 10% 1-methyl-2-pyrrolidone and 5% Kolliphor ® EL

(SIGMA, C5135) in sterile water. Mice bearing MDA-MB231 or LLC tumors of 50–100 mm^3 were administered with vehicle of FABP4 Inh alone (40 mg/kg/day), in combination with TKI (sunitinib) or after treatment cessation at indicated periods. Cisplatin (Calbiochem-CA 15663-27-1, SIGMA, 232120) was dissolved in DMSO at 2 mg/ml and diluted 140X in sterile PBS for use in mice. RSL3 (Selleckchem, S8155), was dissolved in a vehicle composed of (2% DMSO, 30% PEG300, 2% Tween 80, ddH_2O).

2.5. *shRNA transduction*

MDA-MB-231 cells were transduced with shRNA lentiviral vectors containing Non-targeted shRNA (NT-ShRNA) (anti-eGFP) or shRNA directed against SCD1 (TRCN#00000337876 = shRNA n°1, TRCN#00003378757875 = shRNA n°2) (Sigma-Aldrich, St-Louis, USA). For mouse LLC cell line, cells were transduced with lentiviral vectors (vv-16.0033) containing Non-targeted shRNA (shNT) (anti-eGFP) (CCGGTACAACAGCCACAACGTCTATCTCGAGATA-GACGTTGTGGCTGTTGTATTTTT) or shRNA directed against SCD1 (TRCN#0000327815 = shRNA n°3, TRCN#0000327889 = shRNA n°4) (Sigma-Aldrich, St-Louis, USA). All transduction experiments and selection with puromycin (0.5 μM) were performed at the GIGA-Viral vectors platform, Liège University, Liège, Belgium.

2.6. *Spheroid assay*

Spheroids were generated by seeding LLC cells (1×10^3) or MDA-MB231 cells (1×10^3) in each well of a non-adherent, round-bottomed 96 well-plates (Greiner BioOne, Kremsmünster, Autria) in DMEM containing 1% FBS and 20% high-viscosity methyl cellulose (Sigma Aldrich) or 10% FBS lipid depleted and 25% high-viscosity methyl cellulose (MDA-MB231 spheroids). After 24 h (LLC spheroids) and 48 h (MDA-MB231 spheroids) of culture, spheroids were collected, embedded in type I collagen gels at 2 mg/ml (BD Biosciences, San Jose, CA, USA) in 12 well-plates, and maintained in DMEM 1% FBS or DMEM 1% FBS lipid depleted (for MDA-MB231 spheroids) at 37 °C for 24 h. FABP4 and SCD1 inhibitors were diluted into 500 μl of DMEM and added over solid collagen containing spheroids. Cells were examined under a Zeiss Axiovert 25 microscope equipped with an Axiocam Zeiss camera and KS 400 Kontron image-analysis software (Carl Zeiss Microscopy, Zaventem, Belgium).

2.7. *Viability assays*

LLC (1×10^4) and MDA-MB231 (3×10^4) cells were plated in 96 well-plates in DMEM supplemented with 1% FBS or 10% of lipid depleted FBS (BioWest, Riverside, USA). Parental MDA-MB231 and LLC cells were incubated with vehicle, SCD1 Inh, erastin (Selleckchem, S7242) or deferoxamine (DFO) (100 μM) (D9533-1G Sigma) (2 h) or shNT and shSCD1 cells seeded overnight were starved for 1 h in 90 μl DMEM lipid free FBS and incubated with 10 μl of H_2O_2 (100 μM) for 30 min. For experiments using FABP4 Inh, LLC (1×10^4) and MDA-MB231 (3×10^4) cells were plated in 96 well-plates in DMEM supplemented with 1% FBS or 10% FBS, respectively. Parental MDA-MB231 and LLC cells were incubated with vehicle or FABP4 Inh, erastin or DFO for 2 h and incubated with 10 μl of H_2O_2 (100 μM) for 30 min. Viable cells were detected after incubation with 10 μl of 1.90 mg/ml MTS (Promega, Madison, USA).

2.8. *Cell proliferation*

Cell proliferation was assessed using CYQUANT assay according to the manufacture's protocol. For cell proliferation assessment by IncuCyte®, LLC (1×10^{4}) and MDA-MB231 (3×10^{4}) cells were plated in 96 well-plates with DMEM 1% FBS. Data of proliferating profiles were collected and processed from IncuCyte (Sartorius, Göttingen, Germany).

2.9. *ROS dosage assay*

ROS measurement in cancer cells in vitro was performed using the DCFDA Cellular ROS Detection Assay Kit from Abcam (ab 113851) and according to the manufacture's protocol. MDA-MB231 and LLC cells (25×10^3) were incubated in DMEM supplemented with 10% FBS OVN. Cells were incubated with kit reagents and treated with FABP4 Inh for 2 h prior ROS measurement.

2.10. *NADP/NADPH assay*

NADP/NADPH dosage was performed using a bioluminescent NADP/NADPH-Glo assay kit from Promega (G9081). Tumor lysates (10 mg) were collected in specific buffer and luminescence was measured at 340 nm.

2.11. *Western blot analysis*

Tumors and cell lysates were prepared as previously described in Ref. [19]. Total protein extracts (40 μg) were separated under reducing conditions on 5–15% polyacrylamide gels (depending on the molecular weight) and transferred onto polyvinylidene difluoride membranes (NEN, Boston, MA, USA). Membranes were saturated for 1 h with casein (1%, w/v) in PBS-Tween-20 (0.1%, v/v). Antigenic bands were detected by exposing the membranes to human primary antibodies targeting the following proteins: SCD1 [M38], SCD1 [ab52356, Abcam], TxNIP [D5F3E], Cell Signaling (Beverly, MA, USA), FABP4 [ab13979], GPX4 [ab231174] Abcam (Cambridge, England), SOD1 [8B10], Catalase [PA5-23246] Thermofisher (Rockford, IL, USA), GPX1 [A0873] and serotransferrin [A1448] (Abclonal, Woburn, MA, USA). After washes, membranes were incubated with a secondary horseradish peroxydase (HRP)-conjugated goat anti-rabbit antibody (1:2000, DakoCytomation) or sheep anti-mouse antibody (1:1000, DakoCytomation). Immunocomplexes were visualized by chemiluminescence reaction on a luminescent image analyzer (LAS-4000; Fujifilm, Wavre, Belgium). For loading control, membranes were stripped and re-incubated with Hsc70 [B-6, sc-7298] antibody (Santa Cruz, CA, USA), or GAPDH [MAB37A] and actin [A2066] antibody (Sigma Aldrich, Saint-Louis, USA).

2.12. *Immunohistochemistry*

Primary antibodies and dilutions used are: Rabbit polyclonal anti-Lyve-1 (1/1000) (Bioconnect, Huissen, Netherlands); rabbit polyclonal anti-Fatty acid synthase (FASN) (1/100) (Cell signaling, #3180); rabbit polyclonal anti-perilipin A (1/500) (ab352, Abcam); rabbit polyclonal anti-carbonic anhydrase 9 (CA-IX) (1/1000) (ab15086, Abcam); mouse monoclonal anti-CD31 (1/40) (ab10559 Abcam); mouse polyclonal anti-SCD1 (1/100) (ab19862, Abcam); FABP4 (1/1200) (ab13979); PLIN2 (1/400) (ab52356, Abcam), Pimonidazole (1/50), GPX4 (1/500) (ab231174, Abcam) and 4-hydroxynonenal (HNE) at 1/500 (ab46545). Slides of 6 μm thick were autoclaved for 11 min at 126 °C in Target Retrieval Solution (DAKO, S1699, Glostrup, Denmark) except for Lyve-1 staining for which slides were incubated for 20 min at 37 °C in trypsin 0,025% (DAKO, S2012). The procedures applied for endogenous peroxidase blockade was an incubation in 3% H_2O_2/H_2O for 20 min. Tissues was saturated by incubation in PBS/bovine serum albumin 10% (Fraction V, Acros Organics, NJ) for 1 h, for the detection of FASN, perilipin A, and CA-IX. For CD31 staining, non-specific sites were blocked after incubation with normal goat serum 100% (NGS) for 30 min at room temperature. For the detection of PLIN2, slides were incubated with animal free blocking solution (Cell Signaling, 15019L) for 20 min at room temperature (RT). For SCD1 and pimonidazole staining, non-specific sites were blocked by incubation with protein block serum free (DAKO, X0909) 10 min at RT. Tumor sections were then incubated with the primary antibodies, at room temperature, for 1 h or OVN à 4 °C for SCD1 staining. After washes in phosphate buffered saline (PBS), the appropriate secondary antibodies conjugated to peroxidase or biotin for 30 min were added: rabbit anti-rat/biotin (diluted 1/300, DAKO), goat anti-rabbit/biotin (diluted 1/400, DAKO), rabbit anti-guinea pig/HRP (diluted 1/50, DAKO), rabbit anti-rat/HRP (diluted 1/400, DAKO) and goat anti-rabbit ENVISION/HRP, goat anti mouse ENVISION/HRP. After washes in PBS, the antibody-antigen complex was visualized by treatment with 3,3′-diaminobenzidine (DAB, DAKO, Glostrup, Denmark). Samples were counterstained with hematoxylin, washed in H2O, dehydrated in graded alcohols and mounted with EUKITT (*Kindler GmbH*, *Ziegelhofstrasse,* Freiburg).

2.13. Immunofluorescent detection of HNE

Detection of 4-hydroxynonenal (HNE) in cancer cells in vitro was performed on coverslips of sh-SCD1 or shNT MDA-MB231 cells incubated or not with H2O2 (100 μM) for 30 min. Coverslips were washed with PBS, fixed with 4% PFA and permeabilized with 0.5% Triton x-100 for 10 min at RT, washed with PBS and incubated with 5% BSA for 20 min at RT. Cells were incubated with anti-HNE antibody (ab46545, Abcam) at 1/500 in 1% BSA/PBS for 1 h at RT. After washing, cells were incubated with donkey anti rabbit/Alexa Fluor 555 (A31572, Invitrogen) at 1/200 for 1 h at RT, and slides were mounted with DAPI Fluoromount G (0100–20, Souther Biothec) and analyzed by fluorescent microscopy (Olympus).

2.14. Measurement of oxygen consumption and extracellular acidification rates

Oxygen consumption rates (OCR) and extracellular acidification rate (ECAR) were measured using a Seahorse XFp Extracellular Flux Analyzer (Agilent) according to the manufacturer's protocol. Cells were seeded in normal growth medium 24 h before measurement at a density of 25×10^3 cells per well for MDA-MB231 cells and 5×10^4 per well for LLC cells. Plates were pre-coated with Cell-Tak™ for LLC cells. One hour before the assay, cells were incubated in unbuffered serum-free DMEM (Basal DMEM, Agilent) pH 7.4, supplemented with 10 mM glucose, 1 mM sodium pyruvate and 2 mM glutamine at 37 °C in a non-CO2 incubator. Measurements of OCR and ECAR were taken before and after sequential injection of mitochondrial inhibitors. The respiratory chain inhibitors are ATP synthase complex inhibitor oligomycin (1 μM), ATP synthesis uncoupler carbonyl cyanide-p-trifluoromethoxyphenylhydrazone (FCCP, 1 μM) and a mix of complex I inhibitor rotenone and complex III inhibitor antimycin A (0.5 μM each). The amount of DNA per well was determined using Hoechst incorporation after cold methanol/acetone fixation. Representative results of one experiment out of three independent experiments are shown.

2.15. RNA extraction and RT-PCR analysis

RNA extraction form MDA-MB231 and LLC tumors collected during treatment with TKIs and at different time points of the tumor reoxygenation phase and The semi quantitative RT-PCR for mFASN, hFASN and primers were described in Ref. [19].

2.16. Label-free MS quantification

The global proteomic analyses performed on MDA-MB231 xenografts treated with vehicle or TKI (sunitinib) and withdrawal was reported in Ref. [19].

2.17. LC-MS based lipidomics

Three tumor samples of MDA-MB231 xenografts of mice treated with vehicle, TKIs (sunitinib and sorafenib) (hypoxia phase), and 7, 14 and 21 days after treatment cessation (re-oxygenation phase) were snap frozen in liquid nitrogen and then were subjected to lipid extraction. Lipid extraction and the subsequent lipid analysis were performed according to our previous report [26]. Briefly, tumor samples were homogenized with 225 μL of MeOH and 25 μL of 500 μg/L dilauroylphosphatidylcholine (PC 12:0/12:0; Avanti Polar Lipids, AL, USA) dissolved in MeOH as the internal standard. After being left on ice, the solution was centrifuged at 16,000×*g* for 5 min at 4 °C, and the extracted solutions were subjected to LC-MS analysis. LC-MS analysis was carried out using a Nexera LC system (Shimadzu Co., Kyoto, Japan) equipped with two LC-30AD pumps, a DGU-20As degasser, a SIL-30AC autosampler, a CTO-20AC column oven and a CBM-20A control module, coupled with an LCMS-8040 triple quadrupole mass spectrometer (Shimadzu Co.). The lipidmic analysis based upon physicochemical properties and/or spectral similarity with public or commercial spectral libraries was performed. Peak picking and integration were automatically carried out using the LabSolutions software (Shimadzu Corp.), and the results were then checked manually. The peak area of each lipid was normalized to that of the internal standard.

2.18. MALDI fourier transform-ion cyclotron resonance MSI analyses

Tissue sections were prepared using a Research Cryostat Leica CM3050 S (Leica Microsystems Wetzlar, Germany) with the cryotome chamber chilled at −25 °C and the specimen holder at −15 °C. Fourteen μm-thick tissue sections were mounted onto ITO-coated microscopic slides (Bruker Daltonics, Bremen, Germany) adapted for MALDI mass spectrometry and dried 2 h in a desiccator. For matrix deposition, purified 1,5-diaminonaphtalene (1,5-DAN) was purchased from Sigma-Aldrich, Saint Louis, MO, USA. 1,5-DAN solution (5 mg/mL in ACN/H_2O/TFA 1:1:0,001) was deposited using a SunCollect automatic sprayer (SunChrom, Friedrichsdorf, Germany) at a flow rate of 5 μL/min [27]. The SunCollect System uses an optimized spray generator to produce extremely small matrix droplets. For data acquisition, mass spectra from whole tumor were acquired using a SolariX Fourier transform mass spectrometer (FTMS) (9.4 T) equipped with a MALDI ion source and a SmartbeamTM II laser (BrukerDaltonics, Bremen, Germany). Images were acquired at 40 μm resolution using FlexImaging 3.0 software (Bruker Daltonics). The MS method was calibrated using a phospholipid standards solution (PC(18:0/18:1)/PC(16:0/14:0)/PE(18:0/18:1)/PE (16:0/18:1); 1:1:1:1 v/v/v/v). MALDI lipid mass spectra were acquired in positive ion mode from 100 laser shots accumulated at each spot. The laser power was set to 18 % and the frequency to 1000 Hz. For broadband detection mode analyses, mass range was set to m/z 100–1500 and time of flight value was 7 ms. Approximately 8 h were required to achieve an image with a 40 μm spatial resolution. For statistical analysis of MALDI imaging data, the raw images were loaded separately in SCiLS Lab v2016 software (SCiLS, Bremen, Germany). Baseline subtraction was performed using the Top Hat algorithm as well as a weak denoising. The spectra were normalized by total ion count (TIC). The algorithm for peak peaking and spectra alignment was used from the skyline spectrum. The peak list was then reviewed in order to remove values selected from noise and to add some missing peaks. ±0.009 Da was set as the interval width value. For principal component analysis (PCA) analysis, spectra from whole tumor sections were compared. The interval width value was set at ±0.009 Da. Five principal components were set for the calculation and unit variance scaling was used. The analysis was performed in individual spectrum mode. The score plots (spectra) were reported in three dimensions against the three first components.

2.19. Bioinformatics analysis

FABP4 and SCD mRNA expression levels in different cancers and the corresponding normal tissues were obtained from GEPIA, an interactive web server for analyzing the RNA sequencing expression data of 9736 tumors and 8587 normal samples from the TCGA and the GTEx projects. Kaplan–Meier curves were generated with the Kaplan-Meier plotter

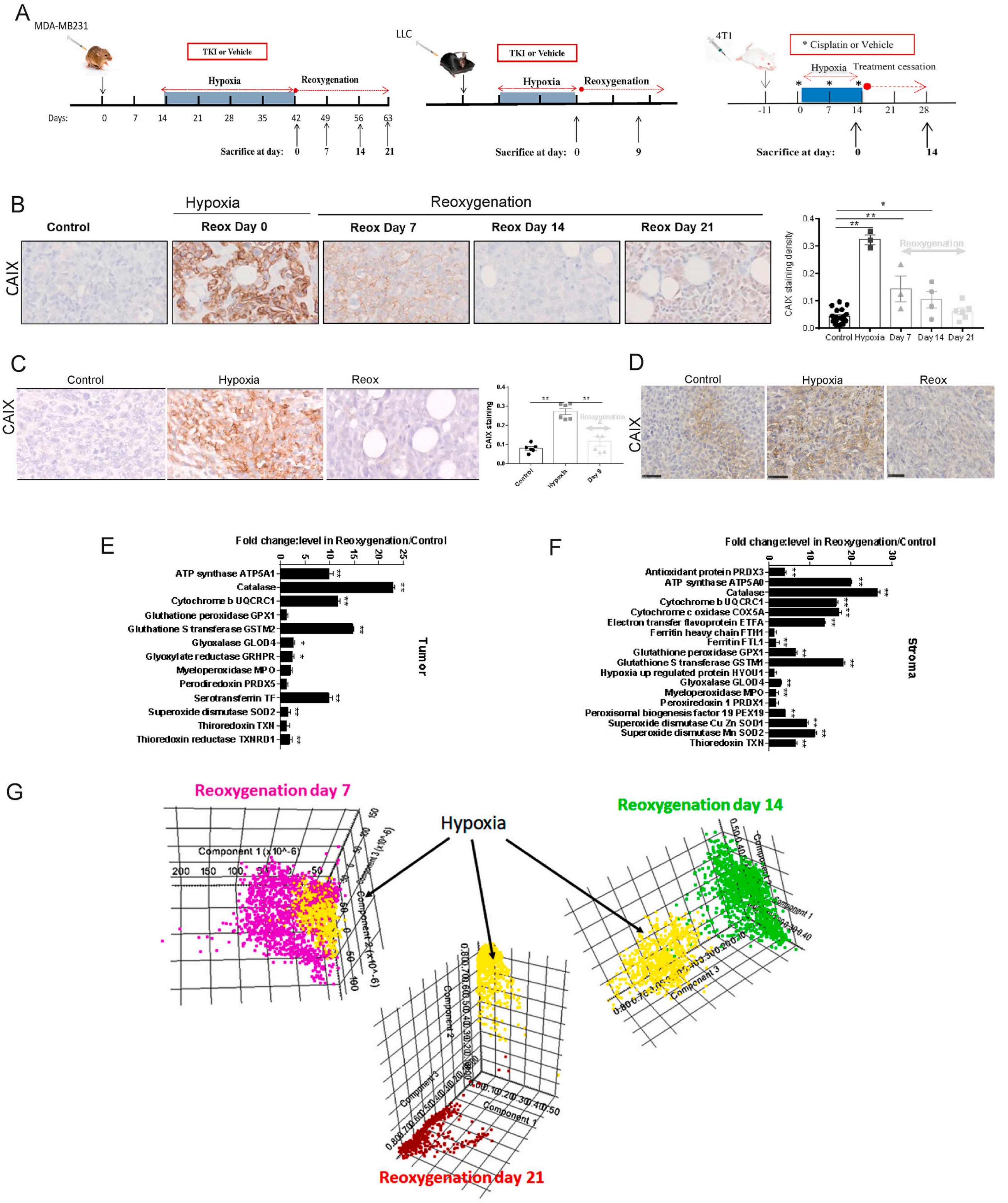

(caption on next page)

Fig. 1. Enhanced oxidative stress and change in the lipogenic profile of residual tumors. (A) Schematic illustration of the in vivo models of hypoxia-reoxygenation. Mice bearing MDA-MB231 or LLC tumors were treated with tyrosine kinase inhibitor (TKI: sunitinib 40 mg/kg/day) for the indicated periods (hypoxia in blue) and then the treatment was stopped (Reoxygenation). Tumors were collected one day after treatment cessation (day 0) corresponding to the hypoxia-phase or at the indicated time points of reoxygenation-phase after treatment cessation (7, 14 and 21 days for MDA-MB231 tumors and 9 days for LLC tumors). For mice bearing 4T1 tumors, mice were treated by i.p. injection of cisplatin (7 mg/kg/week) for 3 weeks and euthanized 3 days after the last injection (hypoxia-phase) and 14 days after treatment cessation and tumor regrowth (reoxygenation-phase). (B,C) Immunohistochemistry analysis of hypoxia by CAIX staining (images) and computerized quantification of CAIX density (graphs) on whole tumor sections of MDA-MB231 xenografts (B) or LLC tumors (C), collected at indicated time points. $^{*}P \leq 0{,}05$; $^{**}P \leq 0{,}01$. (D) Representative images of immunohistochemistry analysis of hypoxia by CAIX staining of 4T1 tumors treated with vehicle (Control), cisplatin (Hypoxia) and cisplatin discontinuation (Reox). (E, F) Global proteomic analysis of oxidative stress markers in MDA-MB231 xenografts during the reoxygenation-phase as compared to vehicle treated tumors. Human (E) and mouse (F) proteins found in tumor stroma were distinguishable and presented separately. Catalase, SOD1, SOD2, glutathione-S-transferase (GSTM1 and GSTM2) and thioredoxin (TXN) were increased in cancer and stromal cells of tumors in the reoxygenation-phase. (G) Mass spectrometry imaging (MALDI imaging) of lipid species on slides of tumor sections revealing differences in the PCA analysis when comparing tumors in hypoxia to tumors after reoxygenation (Reox at day 7, 14 and 21). (For interpretation of the references to color in this figure legend, the reader is referred to the Web version of this article.)

website (http://kmplot.com), using a database of public RNA-Seq datasets. Automatic cut-off scores were selected during queries; overall survival (OS) and relapse free survival (RFS) were selected and log-rank p-values were computed.

2.20. *Image processing and computerized quantification of IHC staining*

Image processing and computerized quantification of IHC staining densities were performed and adapted by using the previously described (14). Histological section images were registered in the full color red, green, bleu (RGB). On those images, blood (CD31), perilipin-I (adipocytes), lipid droplets marker, PLIN2, and FASN, FABP4, SCD1 and GPX4 stainings were visualized as brownish color. Blood vessel and lipid droplet lumens were identified as the lightest structures in the tissue (the value of the threshold depends on the average value of the background). To avoid the selection of other structures (for example, holes in the tissue), only lumens neighboring the detected vessels or lipid droplet walls were considered. It is worth noting that binary images resulting from the image processing described above were systematically compared to the corresponding originals and in the few cases that automatic feature detection was not accurate, threshold was adapted manually. Results are expressed as density of staining defined as the area occupied by these specific detected markers divided by the total area of tumor. Image processing and measurements were performed using the toolbox of image analysis of the MATLAB 9.4 (R2018a) software (Mathworks, Inc.).

2.21. *Statistical analysis*

Considering in vitro experimentation, differences between experimental groups were assessed using a Mann-Whitney test using Prism 7.0 software (GraphPad, San Diego, CA). For computerized images analysis, statistical analysis was performed using the statistic toolbox of Matlab (9.4) 9 (R2018b) software (Mathworks, Inc.). The results were expressed as the mean ± standard error of the mean (SEM). A non-parametric Mann-Whitney significance test was used to compare the median values measured for the groups. Results were considered significant at $p < 0.05$. *In vivo*, to compare differences between mice treatments we used a multiple comparison ANOVA two ways with Holm-Sidak parameter using SigmaPlot software (SYSTAT, San Jose, CA).

3. Results

3.1. *Post therapy mouse residual tumors are enriched in hypoxia and oxidative stress markers and have altered lipid metabolism*

Built on our previous finding that TKI treatment and cessation enhanced *de novo* lipid synthesis and relapse [19], we investigated the impact of hypoxia-reoxygenation on lipid dynamics in tumors. We used xenografts of human triple-negative breast carcinoma MDA-MB231 cells and a syngeneic mouse model of lung cancer (LLC) administered with TKI (sunitinib 40 mg/kg/day) (Fig. 1A) and, the syngeneic model of mouse mammary tumor (4T1) treated with cisplatin (7 mg/kg/week). Tumors were collected at different time points during (Hypoxia) and after treatment discontinuation (Reoxygenation). Assessment of hypoxia induced by treatment was conducted by immunohistochemical (IHC) analysis of the hypoxia marker, carbonic anhydrase 9 (CAIX, also known as CA9), (Fig. 1B, C and D). As expected, a drastic increase in CAIX was revealed during treatments with TKI or cisplatin, referred to herein as the “Hypoxia-phase” (Fig. 1B–D). CAIX production was progressively reduced after treatment cessation, thus reflecting tumor reoxygenation in the “Reoxygenation-phase”.

To check whether hypoxia-reoxygenation is associated with alterations in the redox balance in tumor that might increase tumor aggressiveness, we assessed the levels of oxidative stress markers by proteomic analysis of tumor and stroma proteins derived from MDA-MB231 xenografts (Fig. 1D and E). An increase in the expression of cellular antioxidant defense systems of tumor was obvious with a striking 25-fold change in the human catalase and a 15-fold increase of glutathione-S-transferase-2 (GSTM2) in TKI treated tumors and discontinuation versus vehicle treated tumors (control) (Fig. 1E). Moreover, an increase in mouse catalase (27-fold), GSTM1 (19-fold), SOD1 (10-fold) and superoxide dismutase Mn (SOD2) (12-fold) was detected in the tumor stroma of TKI treated xenografts compared to control (Fig. 1F). Furthermore, a decrease in NADPH pool in tumors confirmed the presence of an elevated oxidative stress in tumors under hypoxia and reoxygenation (Fig. S1A). All together these data indicate a general mobilization of intrinsic antioxidant tumor resources to survive and regrow in oxidative stress amplified by hypoxia/reoxygenation in the TME.

To check for a specific lipid profile in tumors, we applied matrix-assisted laser desorption/ionization (MALDI) Fourier transform-ion cyclotron resonance (FTICR) mass spectrometry-imaging (MSI) analysis to tumor sections of MDA-MB231 tumors during hypoxia and at different time points after reoxygenation (Fig. 1G). Each data point in the plot of the principal component analysis (PCA) represents a mass spectrum corresponding to a particular lipid class. The PCA revealed a strong and progressive shift in the whole lipid profile of tumors from the hypoxia phase to the reoxygenation-phase. This shift in lipid profile detected during reoxygenation-phase was associated with increased expression of fatty acid synthase (FASN) and perilipin-1, a lipid droplet (LD) coating protein and marker of mature adipocytes (Fig. S1B and C). FASN mRNA was induced as early as 2 days after reoxygenation in LLC and 14 days in MDA-MB231 tumors (Fig. S1D and E).

3.2. *Unsaturated fatty acids (FAs) and anti-ferroptotic response are enhanced in residual tumors*

The apparent general shift in the lipid profile prompted us to seek for specific classes of lipids by liquid chromatography-mass spectrometry (LC-MS) analysis of fresh tumor samples (Fig. 2A). Semi-quantitative lipidomic analysis revealed an increase in free fatty acids (FFA) after

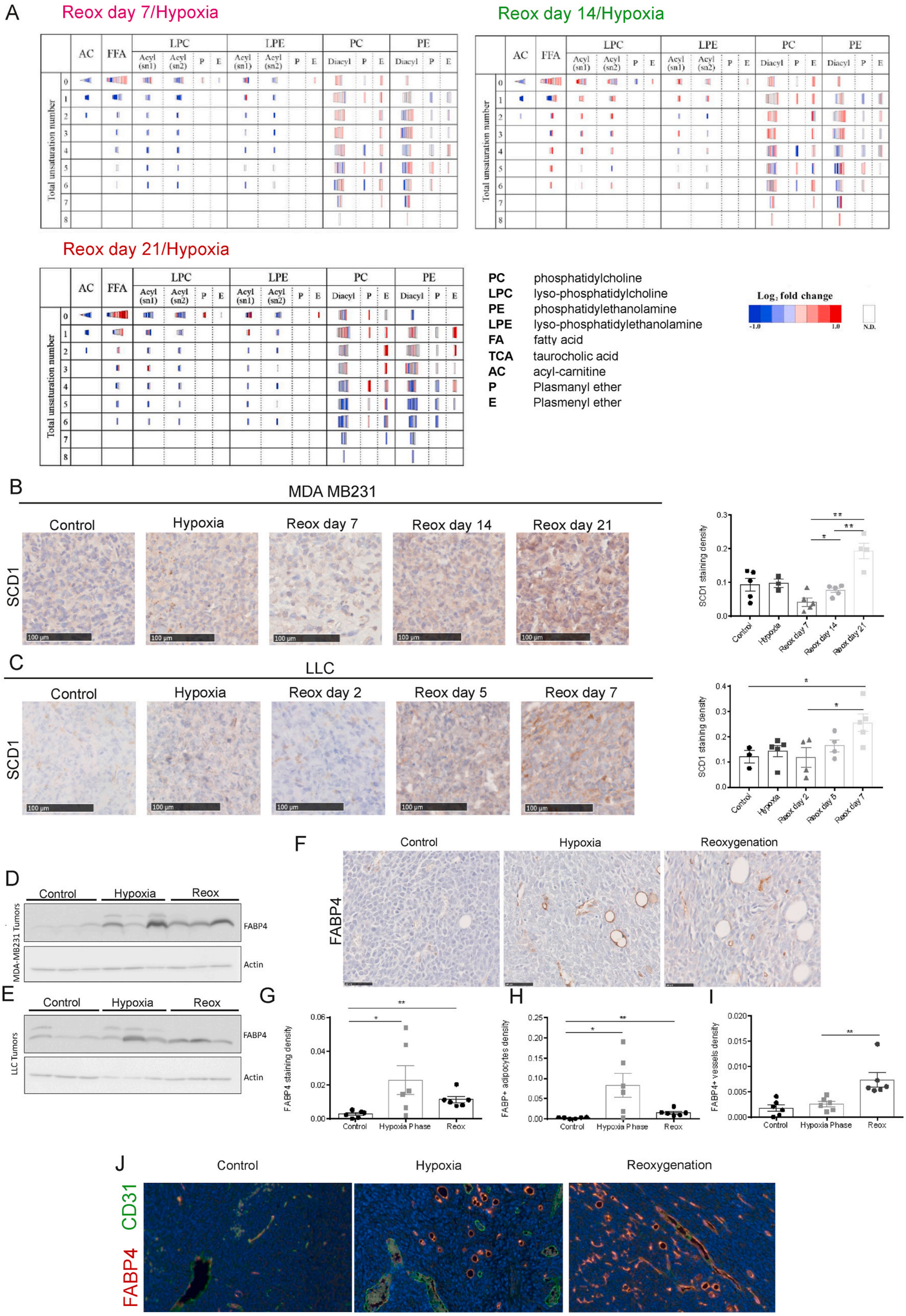

(caption on next page)

Fig. 2. SCD1 and FABP4 are upregulated by hypoxia/reoxygenation in residual tumors (A) Summary of LC-MS analyses of tumors during hypoxia and after different time points of reoxygenation: day 7, 14 and 21. Tables present the lipid profile as ratio between the reoxygenation and the hypoxia phases (red color corresponds to an increase and blue color to a decrease). The vertical axis (0–8) indicates the total unsaturation number. The horizontal axis shows lipid groups and their variants. The length of each bar indicates the total number of carbon atoms. N.D.: not detected; FFA: free fatty acids, Acyl, Diacyl, P (plasmanyl ether) and E (plasmenyl ether) indicate the binding forms of fatty acids. (B, C) Immunohistochemistry analysis (images) and computerized quantification (graphs) of SCD1 staining density in MDA-MB231 (B) and LLC tumors (C) collected at indicated time points. $^{*}P \leq 0,05$; $^{**}P \leq 0,01$. (D, E) Western blot analysis of FABP4 in MDA-MB231 and (D) LLC tumors (E) treated with vehicle or TKI (hypoxia phase) and after treatment cessation (reoxygenation phase: Reox). Actin-beta was used as loading control. (F) Immunohistochemical analysis of FABP4 in LLC tumors treated with vehicle or TKI (hypoxia phase) and after treatment cessation (reoxygenation phase). (G) Computerized quantification of FABP4 staining density in whole tumor sections of tumors in (F). (H) Quantification of FABP4+ adipocytes in tumors. (I) Quantification of FABP4+ blood vessels in tumors. $^{*}P \leq 0,05$; $^{**}P \leq 0,01$. (J) Double-immunofluorescent staining of tumor endothelial cells (TECs) with CD31 antibody (green) and FABP4 (red) showing an increase in FABP4+CD31^{+} cells in tumor after reoxygenation. (For interpretation of the references to color in this figure legend, the reader is referred to the Web version of this article.)

reoxygenation. We also noticed an enrichment of tumors in mono- and polyunsaturated fatty acids (MUFAs and PUFAs) after reoxygenation with a progressive increase in lipid desaturation at day 7, 14 and 21 after TKI cessation. Predominantly, the acyl chains of phosphatidylethanolamine (PE) and Lysophosphatidylethanolamine (LPE) composing cell membranes were enriched in unsaturated FAs in tumors during the reoxygenation-phase. To exclude the possibility that changes of lipid profile were a consequence of the chemical composition of the used TKI (sunitinib), we tested sorafenib, another TKI with a different chemical structure and composition (Fig. S2A). Tumors treated with sorafenib and collected 21 days after reoxygenation displayed similar lipidomic profile as sunitinib treated tumors collected at the same time point (Fig. S2A and B).

Simultaneously, the increase in MUFAs was associated with an upregulation of the Stearoyl-CoA Desatures-1 (SCD1), the key enzyme that inserts double bonds into acyl chains. Detection of SCD1 in tumors by IHC staining revealed its increase during the reoxygenation-phase in both MDA-MB231 (Fig. 2B) and LLC (Fig. 2C) tumors.

Given that enrichment of PUFA in tumors could result from increased lipid uptake from TME, we checked for FA transporters that shuttle PUFA in cancer cells. Interestingly, the lipid transporter FABP4 was upregulated in tumors during hypoxia and reoxygenation-phases as shown by Western blot analysis in MDA-MB231 and LLC tumor lysates (Fig. 2D and E). IHC analysis and quantification of staining density confirmed FABP4 increase in the hypoxic tumors with a sustainable expression during the reoxygenation-phase (Fig. 2F and G). Conversely, FABP4 was not detected in MDA-MB231 or LLC cells cultured in vitro (Fig. S2C), but it was abundant in serum containing medium (Fig. S2D). FABP4 in tumors was mainly immunodetected in adipocytes (Fig. 2H) and tumor endothelial cells (TECs) (Fig. 2I) rather than in cancer cells. In sharp contrast, FABP4 was faintly detected in the stroma of untreated tumors (control). Double IF staining of CD31 and FABP4 confirmed an increase in CD31+/FABP4+ TECs during hypoxia and reoxygenation-phase (Fig. 2J).

The enrichment of MUFA and PUFA in tumors after reoxygenation might support cancer cell membrane fluidity and migration. Nevertheless, PUFA are well-known substrates of iron-mediated lipid peroxidation that induces ferroptotic cell death. We next searched for ferroptosis markers in the proteomic data of MDA-MB231 xenogarfts and found an overall increase in serotransferrin (TF) and aldo-keto-reductase (AKR1c) in cancer (Fig. S2E) and stromal cells (Fig. S2F). Ferritin heavy chain (FTH1), acyl CoA synthetase long chain 1 (ACSL1) and ferritin (FTL1) were found increased only in stromal cells (Fig. S2F). The anti-ferroptosis marker, glutathione peroxidase-1 (GPX1), was 2-fold increased in cancer cells (Fig. S2E), and increased by 17-fold in tumor stroma (Fig. S2F). Notably, heat shock protein beta-1 (HSPB1), the negative regulator of ferroptosis and oxidative stress-induced apoptosis, was downregulated in cancer and stromal cells. Overall, these data indicate a tumor anti-ferroptotic response to lipid and ROS overload during recurrence.

3.3. SCD1 and FABP4 are associated with recurrence of mouse and human cancers

To check whether an anti-cancer drug different from TKI can induce increased expression of SCD1 and FABP4 in tumors, we used cisplatin on syngeneic mouse 4T1 tumors in BALB/c mice as illustrated in (Fig. 1A). Similar to TKI, cisplatin administration reduced tumor growth, whereas treatment cessation was associated with a tumor flair-up and rapid regrowth after drug discontinuation (Fig. 3A). Analysis of FABP4 expression pattern by IHC on tumor sections showed an increase of TECs FABP4 positive cells in the TME during and after treatment, while no staining was revealed in cancer cells (Fig. 3B). Western blot analysis revealed FABP4 expression in 1:5 tumors in vehicle group, 2:5 during drug administration and 4:5 in tumor after regrowth (Fig. 3C), suggesting an enrichment of FABP4 in tumor after treatment. IHC analysis of SCD1 staining in tumors (Fig. 3D) and computerized quantification of SCD1 density in whole tumor sections (Fig. 3E) revealed an increase in SCD1 expression during and after treatment, which indicates a possible role of SCD1 in tumor recurrence after treatment discontinuation.

Given that anticancer drugs, but not restricted to TKI compound, can induce hypoxia and metabolic stress, we assessed the clinical significance of SCD1 and FABP4 expression in a cohort of human tumors, which includes primary tumors and metastatic tissues of patients who showed relapse after first-line chemo or hormone therapy (Fig. 3F–H). Interestingly, IHC analysis of SCD1 (Fig. 3F) and quantification of staining density in whole tumor sections (Fig. 3G) revealed an enrichment of SCD1 in metastatic tissues, while a faint and heterogeneous SCD1 staining was detected in primary tumors. In line with our experimental data in (Fig. 2F and 3B), FABP4 was not detected in cancer cells, but found restricted to blood vessels and adipocytes adjacent to metastatic relapse tissue of human breast cancer (Fig. 3H). Likewise, analyses of RNAseq datasets of TCGA and GTEx confirmed the downregulation of FABP4 mRNA in bulk tumors when compared to normal tissues (Fig. S3A). In contrast, mRNA of SCD1 was found elevated in the majority of human tumors (Fig. S3B). Next, we elucidated the prognostic value of SCD1 and FABP4 in cancer patients by a meta-analysis of public RNA-seq datasets of human cancers. Interestingly, SCD1 expression was associated with decreased recurrence-free survival (RFS) in all analyzed human breast tumors (Fig. 3I) and decreased overall survival (*OS*) of patients with clear renal cell carcinoma, cervical carcinoma (Fig. 3J), lung and bladder cancers, and sarcoma (Fig. S3C). While FABP4 expression was not associated with RFS in breast cancer patients (Fig. 3K), its expression correlated with a decrease in *OS* of head and neck squamous cell carcinoma, lung squamous cell carcinoma (Fig. 3L), stomach adenoma, cervical and breast cancer patients (Fig. S3D).

We then hypothesized that tumor adaptive response to treatment is orchestrated by SCD1 in cancer cells and FABP4 in TME (Fig. 3M). We assumed that TME-derived FABP4 could orchestrate PUFA uptake for lipid droplet (LD) formation in cancer cells, as essential for cell survival under hypoxia and for supplying PUFA in tumors for regrowth. In hypoxia-phase, SCD1 activity in residual tumors is inhibited by the lack of oxygen, whereas reoxygenation boosts its desaturase activity and synthesis of MUFA from saturated fatty acids (SFA), which could

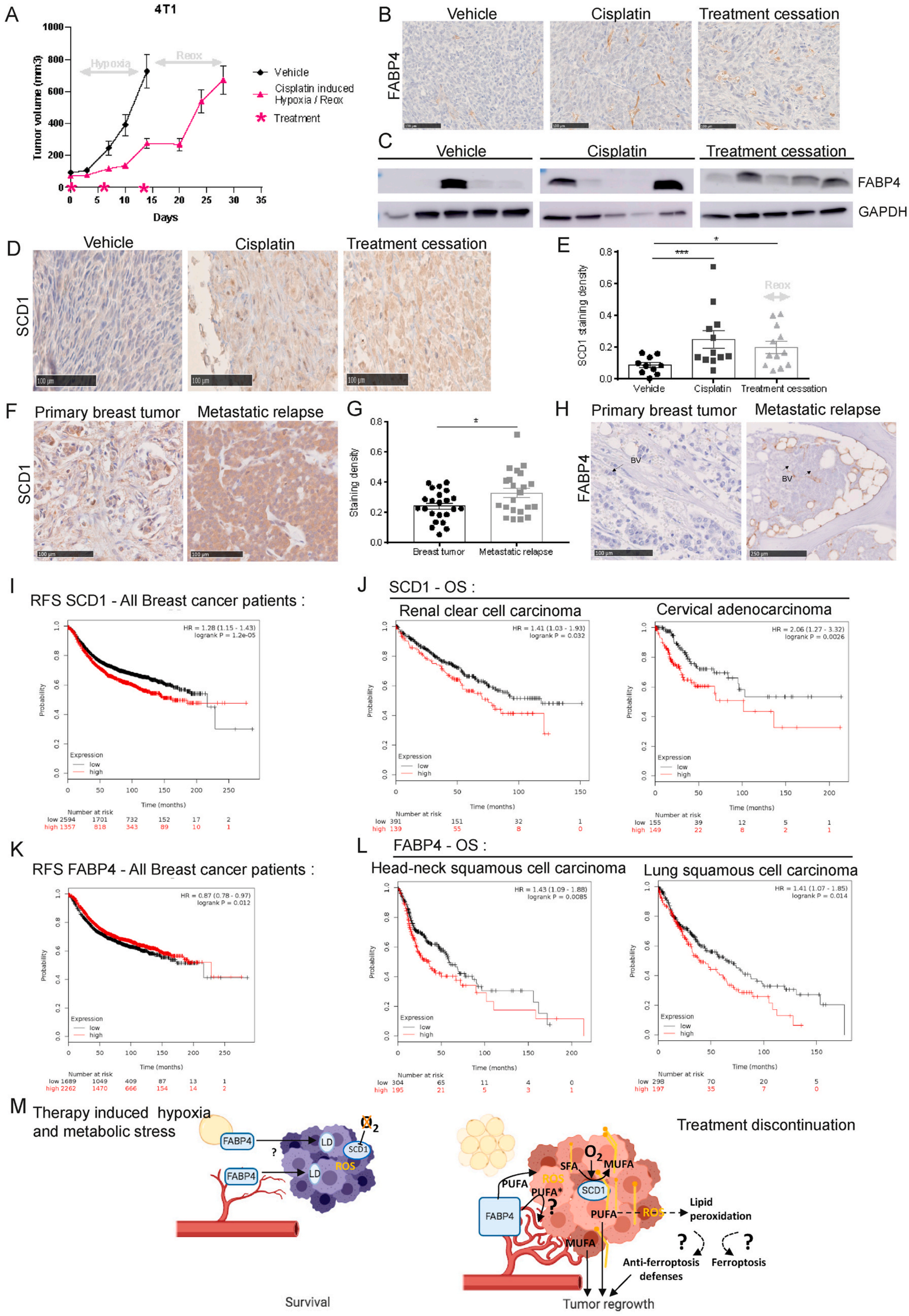

(caption on next page)

Fig. 3. SCD1 in cancer cells and FABP4 in the TME are associated with tumor recurrence in mouse and human cancers. (A) Tumor growth curves of 4T1 tumors in BALB/C mice treated with vehicle or cisplatin (7 mg/kg/week) at the indicated time points (up-arrows). Treatment cessation was associated with a rapid tumor regrowth that reached the volume vehicle tumors after 2 weeks of cisplatin washout. (B) Immunohistochemical analysis of FABP4 in 4T1 tumors treated with vehicle or cisplatin and after treatment cessation. (C) Western blot analysis of FABP4 in 4T1 tumors (n = 5) treated with vehicle or cisplatin and after treatment cessation. GAPDH was used as loading control. (D, E) Images of immunohistochemistry analysis of SCD1 (D) and computerized quantification of SCD1 staining density in 4T1 tumors (E) treated with vehicle, cisplatin or after treatment discontinuation. $^{*}P \leq 0,05$; $^{**}P \leq 0,01$. (F, G) Immunohistochemistry analysis of SCD1 (F) and computerized quantification of staining density (G) on whole tumor sections from human primary breast cancer tumors (n = 23) and their corresponding metastatic relapses (n = 22) after therapies (image showing metastasis in lymph node). $^{*}P \leq 0,05$. (H) Immunohistochemistry analysis of FABP4 in human primary breast cancer samples (n = 23and metastatic relapses (n =22) (image showing bone metastasis). Arrows indicate FABP4+ blood vessels (BV). (I) Recurrence-free survival data associated with SCD1 expression levels in human breast cancers. (J) Overall survival (OS) associated with SCD1 expression in the indicated cancers. (K) Recurrence-free survival data associated with FABP4 expression levels in human breast cancers. (L) Overall survival (OS) associated with FABP4 expression in the indicated cancers. (M) *Working hypothesis*. **Left:** Residual tumors have enhanced ROS levels and increased expression of FABP4 in TECs and in adipocytes, while SCD1 activity is inhibited by the absence of oxygen. Thus, FABP4 may contribute to lipid uptake and LD formation in cancer cells and survival of residual tumors. **Right:** Reoxygenation boosts SCD1 activity and MUFA synthesis in cancer cells, along with the sustained expression of FABP4 in TME that can improve PUFA uptake. Lipid mobilization/desaturation and ROS may influence the tumor redox balance, ferroptosis and recurrence. *Abbreviations: SFA, saturated fatty acids; MUFA, mono unsaturated fatty acids; PUFA, polyunsaturated fatty acids, PUFA*, free radical of PUFA.*

promote recurrence.

3.4. FABP4 in the TME sustains lipid droplet (LD) formation and promotes cancer cell survival under hypoxia and oxidative stress-induced ferroptosis

To explore the consequence of FABP4-mediated FA transport in tumors, we examined LD formation by IF detection of PLIN2, a LD marker protein (Fig. 4A). Quantification revealed and enrichment of LD PLIN2+ in tumors during hypoxia, but not in the reoxygenation-phase (Fig. 4B). A double IF staining of PLIN2 with an epithelial marker, cytokeratin 7 (CK7) or with an mesenchymal cell marker CD11b, demonstrated that lipid droplets PLIN2+ were present within CK7+ cancer cells, but not in CD11b + mesenchymal cells (Fig. S4A). Moreover, double staining of PLIN2 and pimonidazole in tumors collected from mice injected with pimonidazole, confirmed the increase of LD in hypoxic areas (Fig. S4B). The production of LD by cancer cells in response to hypoxia was validated by BODIPY 493/503, which stains neutral lipids of LD (Fig. 4C). Similarly, formation of LD detected by IF staining of PLIN2 was enhanced in cancer cells incubated in vitro under hypoxia when compared to normoxia (Fig. 4D). Notably, pharmacological inhibition of FABP4 activity, available in culture medium by a FABP4 inhibitor (FABP4 Inh) [25] drastically reduced LD in cancer cells (Fig. 4C and D). A computerized quantification of IF staining of LD PLIN2+ revealed a 6-fold reduction of PLIN2 spots in cells treated with FABP4 Inh under hypoxia when compared to normoxia (Fig. 4E). These data demonstrate a cancer cell adaptive response to hypoxia via increased lipid storage by FABP4 and LD formation in vitro.

To investigate the effect of FABP4 available in culture medium on cancer cell migration and growth in 3D cultures, spheroids formed by MDA-MB231 or LLC cells were embedded in type-I collagen gels and incubated with FABP4 Inh. Interestingly, FABP4 Inh inhibited spheroid growth and expansion in vitro (Fig. 4F and G). Similarly, FABP4 Inh inhibited cancer cell migration in 2D cultures of cells in the presence of mitomycin, an inhibitor of cell proliferation (Fig. 4H). Nevertheless, FABP4 Inh did not affect proliferation of LLC (Fig. S4C) and MDA-MB231 cells (Fig. S4D) incubated in 2D culture conditions.

Disruption of LD has been reported to increase ROS in cancer cells [28]. We then tested whether inhibition of lipid uptake by FABP4 Inh that was shown to inhibited LD formation (Fig. 4D and E) could affect ROS levels in cancer cells in vitro. Interestingly, FABP4 inhibition resulted in a dose-dependent increase in ROS production in MDA-MB231 and LLC cells (Fig. 4 I). Notably, incubation of cancer cells under hypoxia in vitro (Fig. 4J) phenocopied the hypoxic and oxidative stress found in vivo (Fig. 1E). Analysis of oxidative stress and ferroptosis markers by Western blot and quantification revealed an increase in TxNIP, catalase and the anti-ferroptotic protein, GPX4, in MDA-MB231 and LLC cells incubated under hypoxia versus normoxia conditions (Fig. 4J). Inhibition of FABP4 enhanced the steady-state level of TxNIP and GPX4 in MDA-MB231 cells and TxNIP in LLC cells incubated under normoxia, while their expression was not potentiated more by FABP4 Inh under hypoxia (Fig. 4J). We next assessed cancer cells response to ROS in vitro after 30 min treatment with H_2O_2 (100 μM) and reporting their viability rate to control condition. Viability rate of MDA-MB231 (Fig. 4K) or LLC (Fig. 4L) cells was reduced by 40% by H_2O_2 that was restored by NAC. Incubation with the ferroptosis inducer, erastin (10 and 20 μM), that blocks the cystine uptake, enhanced cell death in MDA-MB231 than LLC cells, which appears less sensitive to this agent. Interestingly, FABP4 Inh (5 and 10 μM) enhanced MDA-MB231 (Fig. 4M) and LLC (Fig. 4N) cells sensitivity to H_2O_2 and reduced their viability. We then examined whether the observed reduction in cell viability is due to a ferroptotic cell death by using deferoxamine (DFO), a non-toxic iron chelator that inhibits ferroptosis (Fig. 4O and P). Interestingly, DFO resorted cell viability of MDA-MB231 (Fig. 4O) and LLC (Fig. 4P) cells incubated with H_2O_2 and erastin or FABP4 Inh. Altogether, this data suggest that inhibition of FABP4-dependent lipid transport and uptake increased cancer cell sensitivity to ROS-induced ferroptotic cell death.

3.5. SCD1-dependent production of MUFA promotes cell migration and protects cancer cells from oxidative stress-induced ferroptosis

We next determined the functional significance of SCD1 found expressed in cancer cells by its i) pharmacological inhibition with SCD1 inhibitor (SCD1 Inh) [24] and ii) and by its knockdown by using shRNAs in vitro. Human (shRNA#1 and shRNA#2) and mouse (shRNA#3 and shRNA#4) shRNAs-SCD1 efficacies were compared to that of a control shRNA (NT-shRNA) (Fig. 5A). SCD1 Inh slowed spheroid growth and expansion in 3D culture compared with vehicle treatment (Fig. 5B and C). Similarly, down-regulation of SCD1 expression by shRNA reduced spheroid growth and migration in 3D culture compared to control NT-shRNA (Fig. 5D and E). Interestingly, spheroid growth and migration was rescued by the exogenous (C16:1) palmitoleic acid (PA) in SCD1-depleted cells (shRNAs) (Fig. 5F). Suggesting that SCD1 dependent MUFA production in cancer cells could affect their membrane fluidity, migration, proliferation and metabolic capabilities. SCD1 downregulation was associated with a lower oxygen consumption rate (OCR) in cells expressing shRNA-targeting SCD1 under basal conditions and after FCCP challenge in the seahorse assays (Fig. 5G and H). Also, SCD1 inhibition resulted in a drop of cell energy that was revealed by ATP-linked OCR and by reduced basal and maximal respiration capabilities (Fig. S4E, F). While SCD1-depleted MDA-MB231 cells did not show any change in ECAR under an induced energy demand (baseline versus stressed phenotype) (Fig. S4G), a slight decrease of ECAR baseline levels was noticed in LLC cells under the same stress conditions (Fig. S4H). These data suggest a role of SCD1 in sustaining high-energy demand of highly proliferating cancer cells. We further assessed real-time 2D cell proliferation by IncuCyte® instrument and observed a

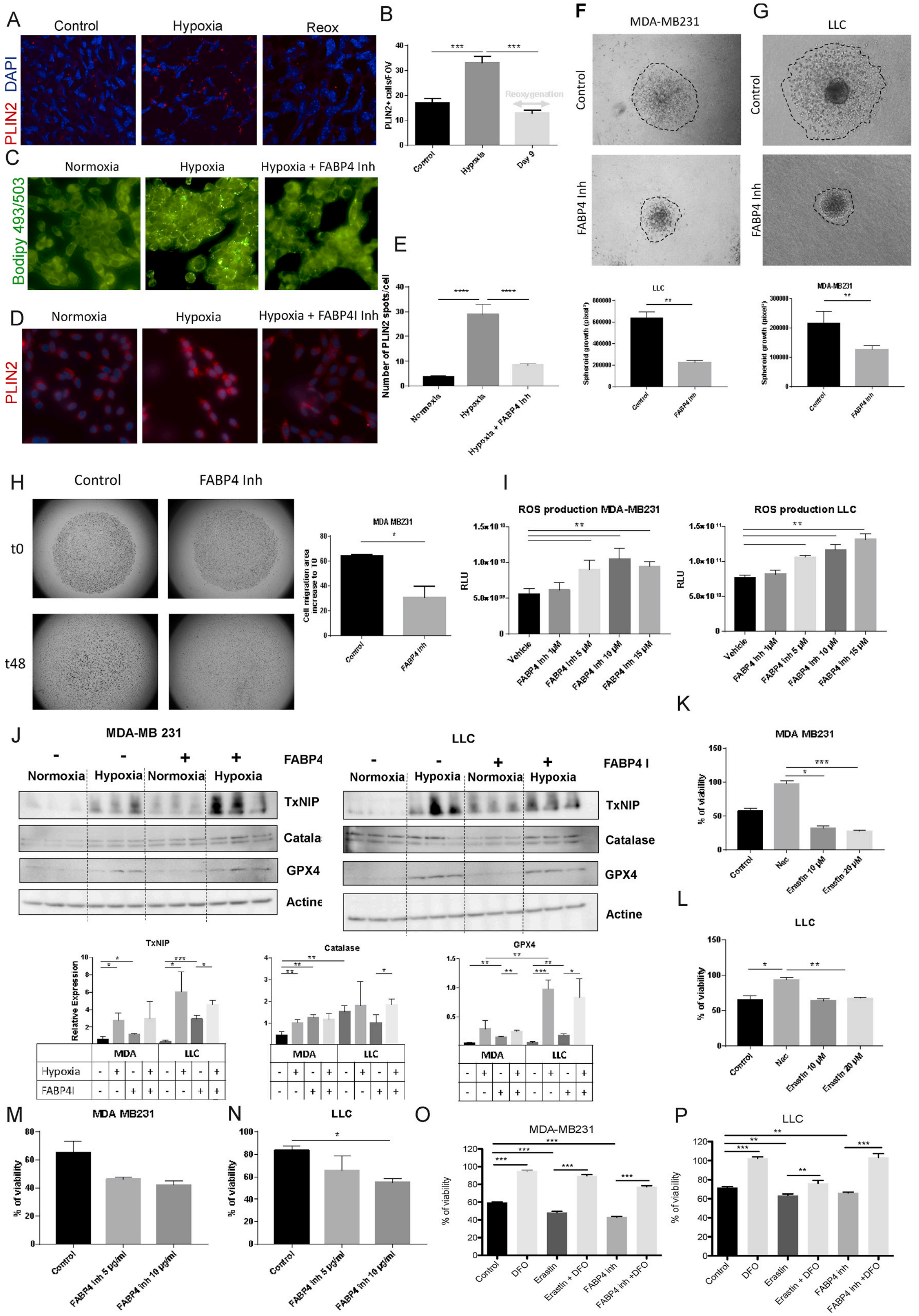

(caption on next page)

Fig. 4. FABP4-induced cancer cell migration, lipid droplet (LD) formation in hypoxia and increased cancer cell resistance to ROS-induced ferroptosis. (A–B) Immunofluorescence detection (A) and computerized quantification (B) of the PLIN2 in LLC tumors treated with vehicle or TKI (Hypoxia-phase) and after treatment cessation (Reoxygenation-phase) (n = 5). (C–E) MDA-MB231 cells were incubated under hypoxia or normoxia for 24 h with or without FABP4 inhibitor (FABP4 Inh) (10 μM). Cells were stained for LD with bodipy 493–503 in green (C) or stained through IF for PLIN2 (D). The graph corresponds to the mean number of PLIN2 spots per cell normalized to DAPI (E). (F, G) Spheroids formed by MDA-MB231 (F) or LLC (G) cells were incubated with vehicle or FABP4 Inh (10 μM) for 24 h and spheroid size was quantified using computerized image analysis (n = 4). (H) The migration of MDA-MB231 cells was assessed in glass inserts in the presence of mitomycin. Cells were incubated with vehicle or FABP4 Inh (10 μM) and allowed to migrate for 48 h. Graph corresponds to the quantification of cell surface area occupied by migrating cells as percentage by subtracting the surface area occupied at time t0 (n = 3). (I) Measurement of ROS levels in MDA-MB231 and LLC cells treated in vitro with increasing concentrations of FABP4 Inh (1–15 μM). (J) Western blot analysis of oxidative stress (TXNIP and catalase) and ferroptosis (GPX4) markers in MDA-MB231 (left) and LLC (right) cells incubated under normoxia or hypoxia, and treated or not for 24 h with FABP4 Inh (10 μM). Graphs correspond to densitometry quantifications of western blots for TxNIP, catalase, and GPX4 (n = 3). (K, L) Cell viability of MDA-MB231 (K) and LLC (L) cells pretreated for 2 h with vehicle (control), N-acetyl cysteine (NAC) or erastin and incubated for 30 min with H2O2 (100 μM). % of viability was determined by the ratio of cell incubated with H2O2/untreated cells (n = 4). (M, N) Cell viability of MDA-MB231 (M) and LLC (N) cells after pharmacological inhibition of FABP4 by FABP4 Inh (5 and 10 μM) for 2 h and incubation with H2O2 (100 μM) for 30 min. % of viability was determined by the ratio of cell incubated with H2O2/untreated cells (n = 4). (O, P) Cell viability of MDA-MB231 (O) and LLC (P) cells pretreated for 2 h with deferoxamine (DFO) (100 μM), erastin (10 μM) and FABP4 Inh (10 μM) and incubated for 30 min with H2O2 (100 μM). % of viability was determined by the ratio of cell incubated with H2O2/untreated cells (n = 4). Statistical analysis was performed with Matlab software for LD counting in (A) and *ANOVA* for (E–P). $^*P \leq 0,05$; $^{**}P \leq 0,01$; $^{***}P \leq 0,001$. (For interpretation of the references to color in this figure legend, the reader is referred to the Web version of this article.)

reduction of cell proliferation upon SCD1 knockdown by SCD1-shRNAs with a more striking effect after its pharmacological inhibition by SCD1 Inh at 5 and 10 μM (Fig. 5I-L).

Given that SCD1 was found upregulated in cancer cells within an oxidative TME, we tested its role in cancer response to oxidative stress in vitro. Pharmacological inhibition or knockdown of endogenous SCD1 by shRNA sensitized MDA-MB231 (Fig. 5M,N) and LLC (Fig. 5O, P) cells to H_2O_2 and reduced cell viability. The reduced viability induced by H_2O_2 (100 μM) and erastin (10 μM) or SCD1 Inh (10 μg/ml) was restored by DFO in MDA-MB231 (Fig. 5Q) and LLC cells (Fig. 5R), indicating a ferroptotic cell death. Altogether, these data demonstrate that SCD1 confers cancer cells with pro-migratory, proliferative and protection from oxidative stress and ferroptosis in vitro.

3.6. *Lipid transport and desaturation promote tumor recurrence in an altered TME*

To explore the cancer therapeutic potential of combining TKI with FABP4 or SCD1 inhibition in vivo (Fig. 6), we tested the effect of pharmacological inhibition of FABP4, (FABP4 Inh), as single agent or in combination with TKI or vehicle in mice bearing LLC or MDA-MB231 tumors (Fig. 6A and B). As reported previously [19], TKI administration in the two experimental models resulted in tumor growth inhibition and rapid tumor regrowth after treatment cessation (Reox). Primary MDA-MB231 tumors were insensitive to FABP4 Inh (Fig. 6A), whereas primary LLC tumors were highly sensitive to FABP4 inhibition (Fig. 6B). In contrast, tumor regrowth after reoxygenation (Reox) was inhibited in MDA-MB231 xenografts and partially affected by FABP4 Inh (Fig. 6A and B). The distinct sensitivity to FABP4 Inh in the two models is likely due to differences in the growth properties and early onset of hypoxia in LLC tumors that was revealed by the use of pimonidazole in vivo and IHC analysis of tumor sections (Fig. S5A, B). Large hypoxic areas were revealed in LLC tumors (Fig. S5B), 21 days after tumor injection, whereas 43 days were required for MDA-MB231 tumors (Fig. S5A). Overall, these data suggest that inhibition of FABP4 in TME reduces the growth of hypoxic tumors, but partially reduces the regrowth. We next explored the potential of targeting SCD1 by its downregulation by shRNA or by its pharmacological inhibition in tumors (Fig. 6C-F). Endogenous silencing of SCD1 by shRNA in both MDA-MB231 and LLC xenografts (Fig. 6C and D) resulted in a striking inhibitory effect on primary tumor growth and regrowth. Pharmacological inhibition of SCD1 did not affect MDA-MB231 primary tumors (Fig. 6E). Combination of SCD1 inhibitor with TKI in the hypoxia-phase and after TKI discontinuation (Hypoxia + SCD1 inh/Reox) reduced tumor regrowth. In LLC tumors SCD1 inh reduced primary tumors and delayed tumor regrowth when combined with TKI (Hypoxia + SCD1 inh/Reox) and after TKI discontinuation in the reoxygenation phase (Hypoxia/Reox + SCD1 inh) (Fig. 6F).

Interestingly, IHC analysis of GPX4 on tumor sections of LLC tumors (Fig. 6G) and quantification (Fig. 6H) revealed an increase in this anti-ferroptotic protein during tumor regrowth in the reoxygenation phase that was strikingly suppressed by SDC1 inh and FABP4 Inh in vivo (Fig. 6G). These data indicate that SCD1 and FABP4 sustained resistance to ferroptosis in part through downregulation of GPX4 in an oxidative TME. Furthermore, a link between SCD1 and FABP4 activity and intrinsic expression of oxidative stress and anti-ferroptotic proteins in human tumors was explored by the analysis of publicly available data (Fig. S5C). We found that SCD1 and FABP4 expression positively correlated with the anti-ferroptotic protein GPX4 (Fig. S5C). This analysis revealed also that SCD1 correlated with SOD1, and FABP4 correlated with TXNIP in human tumors. The pro-ferroptotic effect of SCD1 inhibition in vivo was then validated by the IHC analysis of the lipid peroxide end product, 4-hydroxynoneal (HNE), in tumor sections (Fig. 6I). IHC analysis showed an intense deposition of HNE in cancer cells in the reoxygenation-phase versus hypoxia or control (vehicle) with more staining in shSCD1 tumors when compared to shNT tumors. HNE staining was elevated in hypoxia-phase (TKI) when compared to control (vehicle), but no significant difference was detected between shSCD1 and shNT tumors (Fig. 6I). Furthermore, Incubation of shSCD1 and shNT cells under normal or oxidative stress (H2O2) conditions followed by IF detection of HNE, showed a striking increase of HNE in SCD1-depleted MDA-MB231 cells under oxidative stress, whereas to signal was found in control shNT cells or cells incubated under normal conditions (Figure S5D). All together, these in vivo and in vitro data demonstrate that SCD1 expression endows cancer cells with a powerful protection form ROS-induced ferroptosis.

To unravel a potential link between tumor regrowth and resistance to ferroptosis, we assessed the effect of RSL3, the GPX4 inhibitor, in hypoxia/reoxygenation model of LLC tumors. RSL combination with TKI and its continuation in the reoxygenation-phase (Hypoxia + RSL3/Reox + RSL3) partially reduced tumor regrowth, whereas it has not effect on tumor regrowth when administered only in the reoxygenation-phase (Hypoxia/Reox + RSL3) (Fig. 6J). These data indicate a potential intrinsic resistance of LLC tumors to the classical ferroptosis inducer, RLS3. Interestingly, combination of FABP4 Inh and SCD1 Inh (Fig. 6K) resulted in a more efficient inhibition of LLC tumor regrowth than RSL3 (Fig. 6J).

Overall, we demonstrate that intrinsic lipid desaturation by SCD1 in cancer cells and the lipid transport by stromal-derived FABP4 reinforce tumor detoxification systems and promote cancer progression (Fig. 6L). Collectively, these data provide evidence of residual tumor adaptive response to hypoxia and ROS-enriched environment by FABP4 and SCD1, which promote cancer regrowth (Fig. 6L). Lipid mobilization and desaturation in an altered TME support tumor resistance to ferroptosis

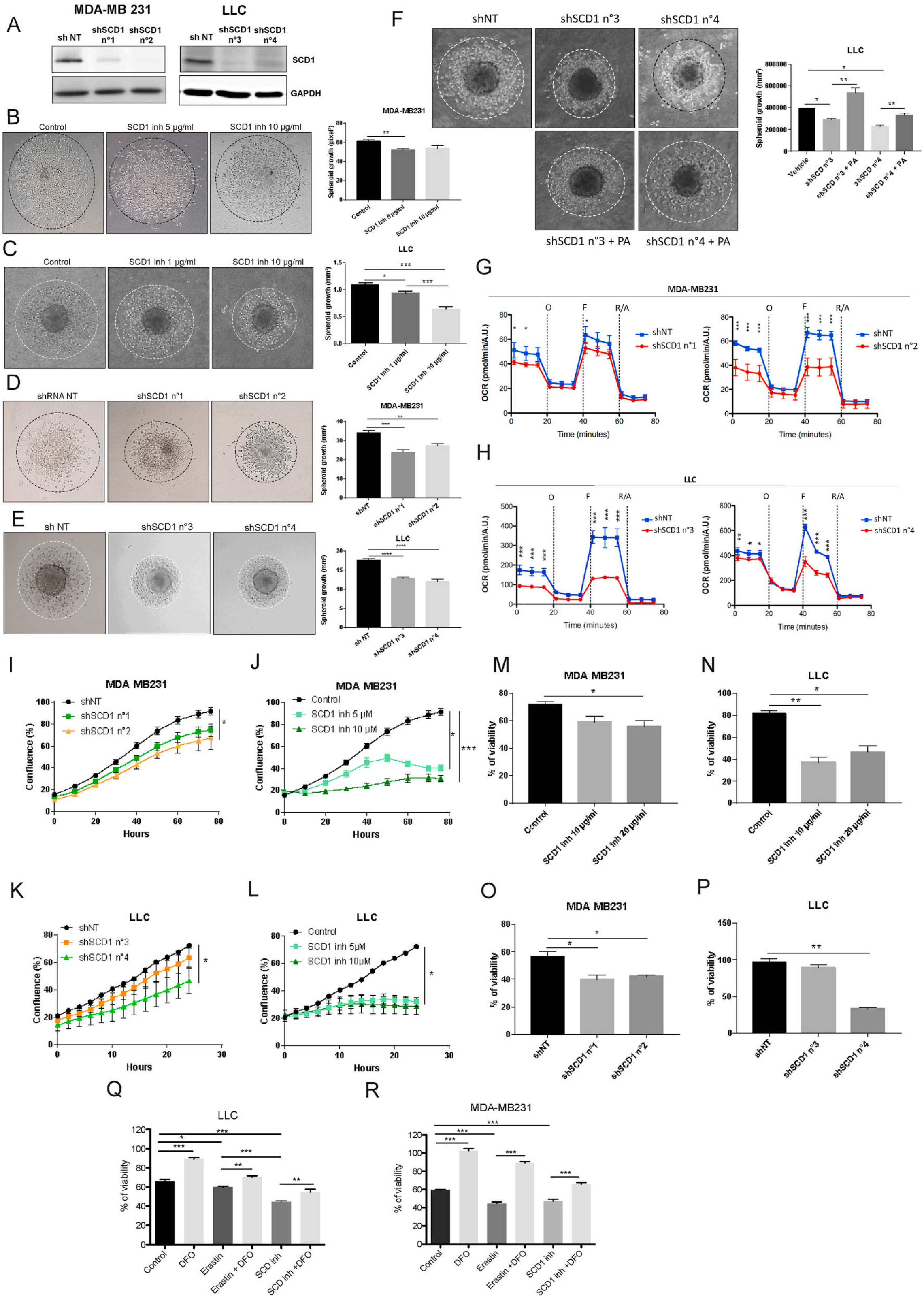

(caption on next page)

Fig. 5. Cancer cell-derived SCD1 enhanced cell migration and protection from ROS-induced ferroptosis (A) Western blot analysis of SCD1 expression in LLC and MDA-MB231 cells incubated with shRNA against SCD1 (shSCD1) and control shRNA (shNT). (B, C) Inhibition of spheroid growth of MDA-MB231 (B) and LLC cells (C) by SCD1 inhibitor (SCD1 Inh). (D, E) Inhibition of spheroid growth by shRNA directed against SCD1: shSCD1 n°1 and n°2 for MDA-MB231 cells (D); shSCD1 n°3 and n°4 for LLC cells (E) compared to their respective control cells (shNT). Graphs are the quantifications of spheroid growth diameter (mm^3) (n = 3). (F) Spheroid formed by LLC cells expressing shSCD1 (n°3 and n°4) were supplemented or not with unsaturated fatty acids (C16:1), palmitoleic acid (PA), in culture media. Graphs are the quantifications of spheroid growth diameter (mm^3) (n = 3). (G, H) Seahorse analyses of oxygen consumption rates (OCR) upon SCD1 depletion. Kinetic OCR response of MDA-MB231 (G) and LLC (H) cells (transduced with control shRNA (shNT) or anti-SCD1 shRNAs after incubation with oligomycin (O, 1 μM), FCCP (F, 1 μM), rotenone and antimycin A mix (R/A, 0.5 μM each). Seahorse assay readouts were normalized to cell number using Hoechst incorporation (arbitrary unit, A.U.). Data are presented as mean ± SD, (n = 3). (I, J) Cell proliferation assessment by Incucyte of MDA-MB231 cells expressing shRNAs directed against SCD1 or control shRNA (shNT) (I), and in (J) by pharmacological inhibition of SCD1 by SCD1 Inh. (K, L) Cell proliferation assessment by IncuCyte® of LLC cells expressing shRNAs directed against SCD1 or control shRNA (shNT) (K), and in (L) by pharmacological inhibition of SCD1 by SCD1 Inh. (M, N) Cell viability of MDA-MB231 (M) and LLC (N) cells after pharmacological inhibition of SCD1 by SCD1 Inh (10 and 20 μg/ml) for 2 h and incubation with H2O2 (100 μM) for 30 min % of viability was determined by the ratio of cell incubated with H2O2/untreated cells (n = 4). (O, P) Cell viability of MDA-MB231 (O) and LLC (P) cells expressing shRNAs directed against SCD1 or control shRNA (shNT) and incubated with H2O2 (100 μM) for 30 min. % of viability was determined by the ratio of cell incubated with H2O2/untreated cells (n = 4). (Q, R) Cell viability of LLC (Q) and MDA-MB231 (R) cells pretreated for 2 h with deferoxamine (DFO) (100 μM), erastin (10 μM) and SCD1 Inh (10 μg/ml) and incubated for 30 min with H2O2 (100 μM). % of viability was determined by the ratio of cell incubated with H2O2/untreated cells (n = 4). $^*P \leq 0{,}05$; $^{**}P \leq 0{,}01$; $^{***}P \leq 0{,}001$.

for regrowth. Finally, inhibition of FABP4 and SCD1 can be proposed as promising potential targets for targeting tumor resistant to ferroptosis and for the design of effective anti-cancer therapies that prevent recurrence.

4. Discussion

The role of metabolic rewiring during in tumor occurrence and resistance to therapeutics are not fully understood. Here, we provide evidence for SCD1 activity in cancer cells and FABP4 activity in TECs and adipocytes as key drivers of tumor growth in an altered TME caused by hypoxia-reoxygenation. By combining lipidomics, proteomics, MALDI-imaging, data mining, in vivo assays with pharmacological inhibitors, in vitro cell-based assays and detoxification systems analyses, we revealed the key role of fatty acid transport and desaturation in tumor survival and regrowth under oxidative stress. More specifically, we found that SCD1 and FABP4 protect tumors from ROS-induced ferroptosis and promote regrowth. Pharmacological inhibition of SCD1 and FABP4 restored ferroptosis and impaired tumor recurrence.

Metabolic vulnerabilities of cancer and endothelial cells were proposed as key targets to combat cancer [29,30], although metabolic heterogeneity and plasticity of tumors may hamper drug efficacy and lead to resistance [31–33]. Besides, changes in TME can greatly influence metabolic pathway [34]and might be a challenge for drugs targeting cancer metabolism. A major aspect of theses changes in TME is tumor hypoxia. While it is well conceived that uncontrolled proliferation overwhelms the existing vessels and causes tumor hypoxia [35], anticancer drugs can exacerbate tumor hypoxia, which can driver drug resistance [36,37]. Previously, we provided evidence of fatty acid addiction of tumors exposed to anti-angiogenics of TKI family [19]. Elevated rate of FASN and lipid synthesis promoted fast tumor regrowth after TKI (sunitinib or sorafenib) cessation. Recently we reported a lipogenic phenotype and enrichment in lipid droplets (LDs) in residual tumors of ovarian cancer xenografts treated with Avastin [38]. Interestingly, lipid metabolism appeared as key driver of drug resistance [39], and FASN has been proven important for cancer cell growth and survival [40]. More recently, FASN activity has been demonstrated as required in sustaining immunosuppressive activity of regulatory T cells in tumors [41]. Though, small-molecule FASN inhibitors (C75 and GSK837149A) have shown promising results in preclinical models [42], but these compounds failed to show efficacy as clinical tools, due to severe toxicities [43]. Alternatively, we found SCD1 and FABP4 are key lipogenic targets of tumor recurrence. Beyond TKI treatment, these two proteins were also upregulated in mouse tumors treated with cisplatin, and in relapses of human breast cancer samples derived from patients treated with chemotherapy or hormone therapy.

Lipid desaturation in cancers has been reported to play a role in drug resistance [17], but its mechanism of action was not described. We demonstrate a new function of SCD1 by which increased MUFA synthesis protects cancer cells from ferroptosis, lipotoxicity of SFA, promotes migration, and stimulates tumor regrowth. Accordingly, SCD1 has been demonstrated as a key target of PI3K-AKT-mTOR pathway by which ferroptosis resistance is triggered in cancer cells [44]. From TME side, we show that FABP4, a known PUFA shuttle [45], promotes migration and protection of cancer cells from ROS-induced lipotoxicity and contributes to tumor recurrence.

Ferroptosis inducers are potential new therapeutics that can reverse drug resistance [15–17]. However, many cancer cells have an intrinsic resistance to ferroptosis inducers [44,46]. We have noticed that LLC cells are less sensitive to erastin, the drug that depletes cysteine in cancer cells by blocking Xc$^-$ system, the antiporter of glutamate/cysteine. While erastin has limited pharmacokinetic activity that prevents its use in vivo, we used RSL3, the anti-GPX4 drug, in an attempt to exacerbate ferroptosis in the reoxygenation-phase. Treatment with RLS3 resulted in a partial inhibition of tumor regrowth after TKI cessation, indicating a potential resistance to RSL3 during the recurrence of LLC tumors. Interestingly, GPX4 expression was reduced in tumors treated by SCD1 and FABP4 inhibitors, supporting that increased MUFA/PUFA availably and dynamics can lower ferroptosis induced by ROS through the expression of GPX4. Accordingly, Inhibition of SCD1 or FABP4 sensitized cancer cells to ROS in vitro through induction of ferroptosis, a process that was validated by the rescue of cell viability by DFO. Remarkably, downregulation of SCD1 showed a strong deposition of HNE in tumors under hypoxia/reoxygenation in vivo and in vitro in cells under oxidative stress, which consolidate the role of SCD1 as key anti-ferroptotic protein.

While FABP4 expression appeared downregulated in several human tumors, we show that pharmacological inhibition of FABP4 efficacy on primary tumor growth is dependent on the occurrence of hypoxia. Upregulation of GPX4 by hypoxia in vitro in two different cell lines (Fig. 4J) demonstrate a cancer cell rapid adaptation to hypoxic stress that was more striking in the highly proliferative and hypoxic LLC cells when compared to MDA-MB231, which may help counter ferroptosis in hypoxia. Accordingly, the highly proliferating and hypoxic LLC primary tumors were more sensitive to FABP4 Inh than MDA-MB231 xenografts. These data point to a potential crucial role of hypoxia in the regulation of ferroptosis in cancer, further future studies are required to elucidate the potential link between HIF1/2α stabilization and regulation of GPX4, FABP4 and ferroptosis in tumor hypoxia. Several reports have demonstrated anti-tumor efficacy of targeting FABP4 by siRNAs, which decreased the occurrence of metastases, in several organs in mice [47]. We noticed an enrichment of FABP4 derived from TME of residual tumors after TKI or cisplatin treatment, while another group reported a key role of FABP3 and FABP7 derived from cancer cells in response to hypoxia-reoxygenation driven by Avastin treatment in glioblastoma [20], suggesting a potential specific role of FABPs derived from different

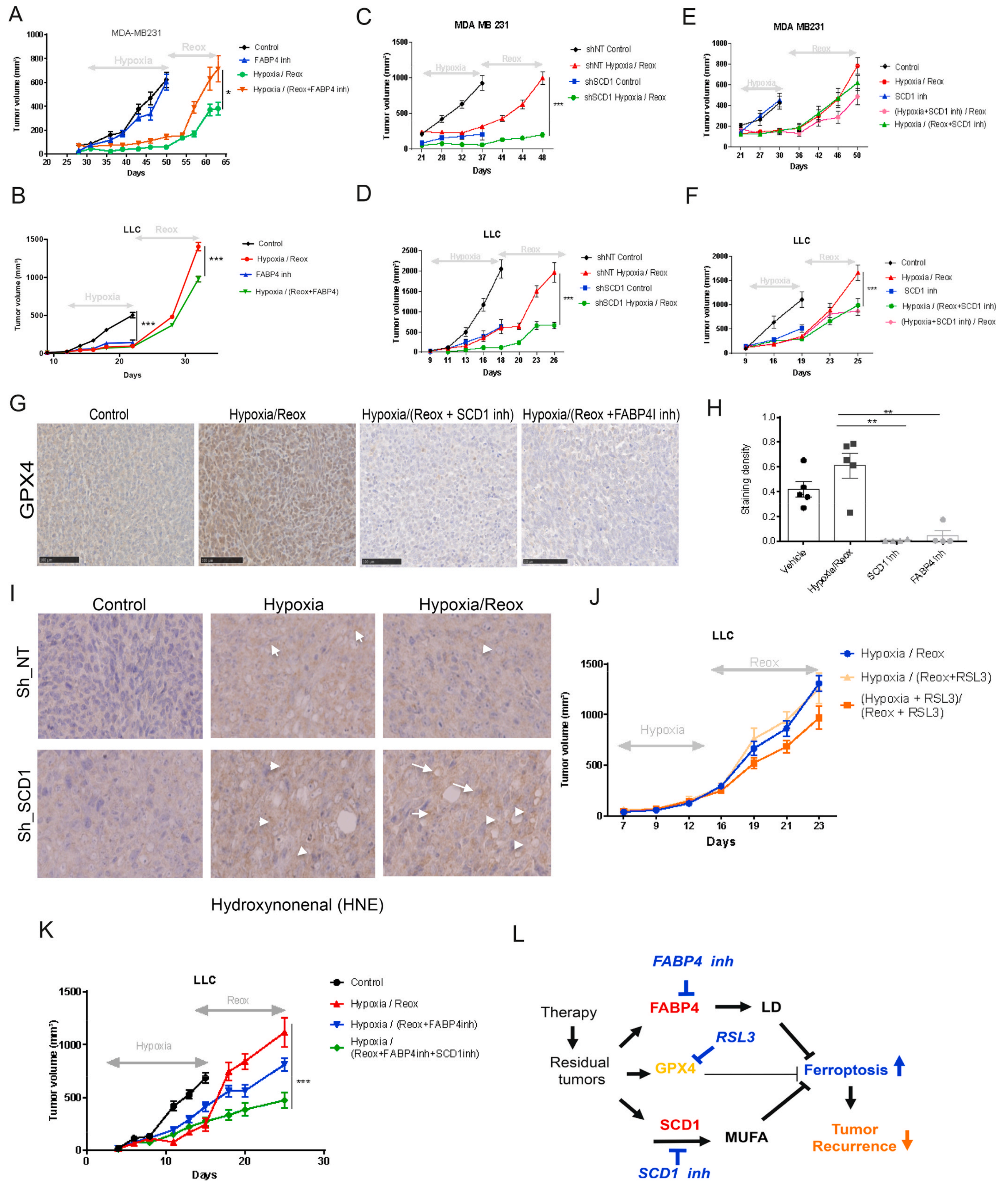

(caption on next page)

Fig. 6. Lipid transport and desaturation drive ferroptosis resistance and tumor recurrence in vivo (A, B) Tumor growth curves of MDA-MB231 xenografts (A) or LLC tumors (B) treated (double headed arrow) with TKI and/or FABP4 Inh (40 mg/kg/day) (n = 6). (C, D) Tumor growth curves of MDA-MB231 xenografts (C) and LLC tumors (D) expressing control shRNA (shNT) or shRNA against SCD1 (n = 6). (E, F) Tumor growth curves of MDA-MB231 xenografts (E) or LLC tumors (F) treated (double headed arrow) with TKI and/or SCD Inh (n = 6). (G, H) Images of IHC analysis of GPX4 (G) and computerized quantification of GPX4 staining density (H) in whole tumor sections of LLC tumors treated with vehicle (control) or TKI treatment and discontinuation (Hypoxia/Reox) in (B and F), followed by SCD1 Inh (hypoxia/Reox + SCD Inh) in (F) or by FABP4 Inh (Hypoxia/Reox + FABP Inh) in (B) (n = 5). (I) Images representative of HNE staining in LLC tumors expressing shRNA against SCD1 or control shRNA (sh-NT) of tumors in (D), including control tumor (vehicle), tumors in hypoxia (TKI) and tumor in Hypoxia/Reox, after TKI cessation. HNE deposition in cancer cells is showed by white arrows in the pictures. (J) Tumor growth curves of LLC tumors in mice treated or not with a combination of RSL3 and TKI (Hypoxia + RSL3/Reox + RSL3) or after TKI cessation (Hypoxia/Reox + RSL3) (n = 5). (K) Tumor growth curves of LLC tumors in mice treated with vehicle, TKI and cessation (Hypoxia/Reox) and followed by FABP4 Inh alone (Hypoxia/Reox + FABP4 Inh) or a combination of FABP Inh with and SCD1 Inh (Hypoxia/Reox + FABP4 Inh + SCD Inh) (n = 6). *P ≤ 0,05; **P ≤ 0,01; ***P ≤ 0,001; ****P ≤ 0,0001 (M) Schematic overviw of the main findings. Residual tumors have increased expression of FABP4 in TECs and adipocytes that sustains LD formation within cancer cells and resistance to ferroptosis. While residual tumors have increased expression of GPX4, they show resistance to RSL3. Reoxygenation of residual tumors promotes lipid desaturation by SCD1 and promotes cell migration and protection from ferroptosis. Inhibition of SCD1 and FABP4 sensitized tumors to ferroptotic cell death and abolished tumor recurrence.

tumor compartments in cancer recurrence. FABP4 was also found expressed in the TME of ovarian cancer and mostly at the adipocyte-tumor cell interface that promotes cancer cell metastasis [48]. While FABP4 expression was restricted to TECs and adipocytes in the TME, we demonstrated its clear contribution in sustaining LD formation in cancer cells under hypoxia. Interestingly, inhibition of FABP4 in vitro, resulted in a disruption of LD and increased ROS and ferroptotic cell death in cancer cells. Whereas FABP4 Inh partially delayed tumor regrowth, its combination with SCD1 Inh was more effective in blocking recurrence of the ferroptosis resistant LLC tumors.

Altogether, we show that SCD1-dependent lipid desaturation in cancer cells and lipid transport in the TME by FABP4, cooperatively drive recurrence after treatment by conferring resistance to oxidative stress and ferroptosis.

5. Conclusions

Tumor occurrence is one of biggest challenge of cancer therapy. Years on ferroptotis research have demonstrated the potential of targeting ferroptosis-associated cancer progression and further explored ferroptosis sensitization to small molecules in primary tumors. Our work provides the first evidence of a tumor adaptive mechanism to ROS and ferroptosis during tumor recurrence. We show that hypoxia-reoxygenation drive this adaptation and point to the role of lipid transport from the TME and lipid desaturation in sustaining tumor regrowth. More investigations on underlying mechanisms by which hypoxia derived factors regulate ferroptosis in resistant tumors, could provide more insights into the problem of recurrence in different cancer types. Overall our results are potentially translatable toward novel therapies targeting FABP4 and SCD1 in tumor resistance and relapse.

Declaration of competing interest

The authors declare no conflict of interests.

Acknowledgments

This work was supported grants (CDR) from the national fund for scientific research (FRS-FNRS) CDR # 31247715, PDR-TLV # 32801162 and by PDR #T.023020 [N.E.S.]. Grants from the Fonds Spéciaux and Credits Sectorials de la recherche and Leon Fredericq Foundation; Liège University, Belgium [N.E.S.]. The lipidomic study was supported by the grant from the AMED-CREST program run by the Japan Agency for Medical Research and Development [M.Y.]. We thank all the members of Sounni and Noel's group, the viral vector, mass spectrometry and the cell imaging and flow cytometry platforms of the GIGA for the useful technical support. We thank the Biobank of Liège University for providing FFPE of breast cancer samples.

Appendix A. Supplementary data

Supplementary data to this article can be found online at https://doi.org/10.1016/j.redox.2021.102006.

Author contributions

N.E.S., A.N., G.L. and A.G., designed the study and interpreted the results. N.E.S. and A.N. supervised the study. N.E.S. wrote the manuscript. G.L., A.G., C·W., L.M., N.M. and A.C. performed the experiments. S.B. performed the image quantification analyses. E.M. performed bioinformatics analyses. J.C., G.M. and E.D. performed the proteomics. J.C. and R.L. performed the Mass Spectrometry Imaging. S.N. and M.Y. performed the lipidomics. A.N., A.B. and E.P. reviewed the paper.

References

[1] D.A. Mahvi, R. Liu, M.W. Grinstaff, Y.L. Colson, C.P. Raut, Local cancer recurrence: the realities, challenges, and opportunities for new therapies, CA, Cancer J. Clin. 68 (2018), https://doi.org/10.3322/caac.21498.

[2] D. Ackerman, M.C. Simon, Hypoxia, lipids, and cancer: surviving the harsh tumor microenvironment, Trends Cell Biol. 24 (2014) 472–478, https://doi.org/10.1016/j.tcb.2014.06.001.

[3] A.L. Harris, Hypoxia–a key regulatory factor in tumour growth, Nat. Rev. Canc. 2 (2002) 38–47. http://www.ncbi.nlm.nih.gov/entrez/query.fcgi?cmd=Retrieve&db=PubMed&dopt=Citation&list_uids=11902584.

[4] C.R. Reczek, N.S. Chandel, The two faces of reactive oxygen species in cancer, Annu. Rev. Cell Biol. 1 (2017) 79–98, https://doi.org/10.1146/annurev-cancerbio-041916-065808.

[5] G. Manda, G. Isvoranu, M.V. Comanescu, A. Manea, B. Debelec Butuner, K. S. Korkmaz, The redox biology network in cancer pathophysiology and therapeutics, Redox Biol 5 (2015) 347–357, https://doi.org/10.1016/j.redox.2015.06.014.

[6] K. Sanna, E.K. Rofstad, Hypoxia-induced resistance to doxorubicin and methotrexate in human melanoma cell lines in vitro, Int. J. Canc. 58 (1994) 258–262. http://www.ncbi.nlm.nih.gov/pubmed/8026888.

[7] L.I. Cardenas-Navia, D. Mace, R.A. Richardson, D.F. Wilson, S. Shan, M. W. Dewhirst, The pervasive presence of fluctuating oxygenation in tumors, Canc. Res. 68 (2008) 5812–5819, https://doi.org/10.1158/0008-5472.CAN-07-6387.

[8] G.L. Semenza, Hypoxia-inducible factors: coupling glucose metabolism and redox regulation with induction of the breast cancer stem cell phenotype, EMBO J. 36 (2017) 252–259, https://doi.org/10.15252/embj.201695204.

[9] J.M. Brown, W.R. Wilson, Exploiting tumour hypoxia in cancer treatment, Nat. Rev. Canc. 4 (2004) 437–447, https://doi.org/10.1038/nrc1367.

[10] C. Zhang, S. Cao, B.P. Toole, Y. Xu, Cancer may be a pathway to cell survival under persistent hypoxia and elevated ROS: a model for solid-cancer initiation and early development, Int. J. Canc. 136 (2015) 2001–2011, https://doi.org/10.1002/ijc.28975.

[11] F. Li, X. Han, F. Li, R. Wang, H. Wang, Y. Gao, X. Wang, Z. Fang, W. Zhang, S. Yao, X. Tong, Y. Wang, Y. Feng, Y. Sun, Y. Li, K.K. Wong, Q. Zhai, H. Chen, H. Ji, LKB1 inactivation elicits a redox imbalance to modulate non-small cell lung cancer plasticity and therapeutic response, Canc. Cell 27 (2015) 698–711, https://doi.org/10.1016/j.ccell.2015.04.001.

[12] A. Kruger, N.M. Gruning, M.M. Wamelink, M. Kerick, A. Kirpy, D. Parkhomchuk, K. Bluemlein, M.R. Schweiger, A. Soldatov, H. Lehrach, C. Jakobs, M. Ralser, The pentose phosphate pathway is a metabolic redox sensor and regulates transcription during the antioxidant response, Antioxidants Redox Signal. 15 (2011) 311–324, https://doi.org/10.1089/ars.2010.3797.

[13] J. Ye, J. Fan, S. Venneti, Y.W. Wan, B.R. Pawel, J. Zhang, L.W. Finley, C. Lu, T. Lindsten, J.R. Cross, G. Qing, Z. Liu, M.C. Simon, J.D. Rabinowitz, C. B. Thompson, Serine catabolism regulates mitochondrial redox control during

hypoxia, Canc. Discov. 4 (2014) 1406–1417, https://doi.org/10.1158/2159-8290.CD-14-0250.

[14] W.S. Yang, K.J. Kim, M.M. Gaschler, M. Patel, M.S. Shchepinov, B.R. Stockwell, Peroxidation of polyunsaturated fatty acids by lipoxygenases drives ferroptosis, Proc. Natl. Acad. Sci. U.S.A. 113 (2016), https://doi.org/10.1073/pnas.1603244113.

[15] W.S. Yang, R. SriRamaratnam, M.E. Welsch, K. Shimada, R. Skouta, V. S. Viswanathan, J.H. Cheah, P.A. Clemons, A.F. Shamji, C.B. Clish, L.M. Brown, A. W. Girotti, V.W. Cornish, S.L. Schreiber, B.R. Stockwell, Regulation of ferroptotic cancer cell death by GPX4, Cell 156 (2014) 317–331, https://doi.org/10.1016/j.cell.2013.12.010.

[16] S.J. Dixon, K.M. Lemberg, M.R. Lamprecht, R. Skouta, E.M. Zaitsev, C.E. Gleason, D.N. Patel, A.J. Bauer, A.M. Cantley, W.S. Yang, B. Morrison, B.R. Stockwell, Ferroptosis: an iron-dependent form of nonapoptotic cell death, Cell 149 (2012), https://doi.org/10.1016/j.cell.2012.03.042.

[17] V.S. Viswanathan, M.J. Ryan, H.D. Dhruv, S. Gill, O.M. Eichhoff, B. Seashore-Ludlow, S.D. Kaffenberger, J.K. Eaton, K. Shimada, A.J. Aguirre, S.R. Viswanathan, S. Chattopadhyay, P. Tamayo, W.S. Yang, M.G. Rees, S. Chen, Z. V Boskovic, S. Javaid, C. Huang, X. Wu, Y.Y. Tseng, E.M. Roider, D. Gao, J.M. Cleary, B. M. Wolpin, J.P. Mesirov, D.A. Haber, J.A. Engelman, J.S. Boehm, J.D. Kotz, C. S. Hon, Y. Chen, W.C. Hahn, M.P. Levesque, J.G. Doench, M.E. Berens, A.F. Shamji, P.A. Clemons, B.R. Stockwell, S.L. Schreiber, Dependency of a therapy-resistant state of cancer cells on a lipid peroxidase pathway, Nature 547 (2017) 453–457, https://doi.org/10.1038/nature23007.

[18] M. Apicella, E. Giannoni, S. Fiore, K.J. Ferrari, D. Fernandez-Perez, C. Isella, C. Granchi, F. Minutolo, A. Sottile, P.M. Comoglio, E. Medico, F. Pietrantonio, M. Volante, D. Pasini, P. Chiarugi, S. Giordano, S. Corso, Increased lactate secretion by cancer cells sustains non-cell-autonomous adaptive resistance to MET and EGFR targeted therapies, Cell Metabol. 28 (2018) 848–865, https://doi.org/10.1016/j.cmet.2018.08.006, e6.

[19] N.E. Sounni, J. Cimino, S. Blacher, I. Primac, A. Truong, G. Mazzucchelli, A. Paye, D. Calligaris, D. Debois, P. De Tullio, B. Mari, E. De Pauw, A. Noel, Blocking lipid synthesis overcomes tumor regrowth and metastasis after antiangiogenic therapy withdrawal, Cell Metabol. 20 (2014), https://doi.org/10.1016/j.cmet.2014.05.022.

[20] K. Bensaad, E. Favaro, C.A. Lewis, B. Peck, S. Lord, J.M. Collins, K.E. Pinnick, S. Wigfield, F.M. Buffa, J.L. Li, Q. Zhang, M.J. Wakelam, F. Karpe, A. Schulze, A. L. Harris, Fatty acid uptake and lipid storage induced by HIF-1alpha contribute to cell growth and survival after hypoxia-reoxygenation, Cell Rep. 9 (2014) 349–365, https://doi.org/10.1016/j.celrep.2014.08.056.

[21] H. Iwamoto, M. Abe, Y. Yang, D. Cui, T. Seki, M. Nakamura, K. Hosaka, S. Lim, J. Wu, X. He, X. Sun, Y. Lu, Q. Zhou, W. Shi, T. Torimura, G. Nie, Q. Li, Y. Cao, Cancer lipid metabolism confers antiangiogenic drug resistance, Cell Metabol. 28 (2018) 104–117, https://doi.org/10.1016/j.cmet.2018.05.005, e5.

[22] C. Corbet, A. Pinto, R. Martherus, J.P. Santiago de Jesus, F. Polet, O. Feron, Acidosis drives the reprogramming of fatty acid metabolism in cancer cells through changes in mitochondrial and histone acetylation, Cell Metabol. 24 (2016) 311–323, https://doi.org/10.1016/j.cmet.2016.07.003.

[23] Z.T. Schug, B. Peck, D.T. Jones, Q. Zhang, S. Grosskurth, I.S. Alam, L.M. Goodwin, E. Smethurst, S. Mason, K. Blyth, L. McGarry, D. James, E. Shanks, G. Kalna, R. E. Saunders, M. Jiang, M. Howell, F. Lassailly, M.Z. Thin, B. Spencer-Dene, G. Stamp, N.J. van den Broek, G. Mackay, V. Bulusu, J.J. Kamphorst, S. Tardito, D. Strachan, A.L. Harris, E.O. Aboagye, S.E. Critchlow, M.J. Wakelam, A. Schulze, E. Gottlieb, Acetyl-CoA synthetase 2 promotes acetate utilization and maintains cancer cell growth under metabolic stress, Canc. Cell 27 (2015) 57–71, https://doi.org/10.1016/j.ccell.2014.12.002.

[24] S. Fanning, A. Haque, T. Imberdis, V. Baru, M.I. Barrasa, S. Nuber, D. Termine, N. Ramalingam, G.P.H. Ho, T. Noble, J. Sandoe, Y. Lou, D. Landgraf, Y. Freyzon, G. Newby, F. Soldner, E. Terry-Kantor, T.E. Kim, H.F. Hofbauer, M. Becuwe, R. Jaenisch, D. Pincus, C.B. Clish, T.C. Walther, R. V Farese Jr., S. Srinivasan, M. A. Welte, S.D. Kohlwein, U. Dettmer, S. Lindquist, D. Selkoe, Lipidomic analysis of alpha-synuclein neurotoxicity identifies stearoyl CoA desaturase as a target for Parkinson treatment, Mol. Cell 73 (2019) 1001–1014, https://doi.org/10.1016/j.molcel.2018.11.028, e8.

[25] G. Floresta, V. Pistara, E. Amata, M. Dichiara, A. Marrazzo, O. Prezzavento, A. Rescifina, Adipocyte fatty acid binding protein 4 (FABP4) inhibitors. A comprehensive systematic review, Eur. J. Med. Chem. 138 (2017) 854–873, https://doi.org/10.1016/j.ejmech.2017.07.022.

[26] Y. Yamashita, S. Nishiumi, S. Kono, S. Takao, T. Azuma, M. Yoshida, Differences in elongation of very long chain fatty acids and fatty acid metabolism between triple-negative and hormone receptor-positive breast cancer, BMC Canc. 17 (2017) 589, https://doi.org/10.1186/s12885-017-3554-4.

[27] B. Heijs, E.A. Tolner, J. V Bovee, A.M. van den Maagdenberg, L.A. McDonnell, Brain region-specific dynamics of on-tissue protein digestion using MALDI mass spectrometry imaging, J. Proteome Res. 14 (2015) 5348–5354, https://doi.org/10.1021/acs.jproteome.5b00849.

[28] X. Cheng, F. Geng, M. Pan, X. Wu, Y. Zhong, C. Wang, Z. Tian, C. Cheng, R. Zhang, V. Puduvalli, C. Horbinski, X. Mo, X. Han, A. Chakravarti, D. Guo, Targeting DGAT1 ameliorates glioblastoma by increasing fat catabolism and oxidative stress, Cell Metabol. 32 (2020), https://doi.org/10.1016/j.cmet.2020.06.002.

[29] M.G. Vander Heiden, S.Y. Lunt, T.L. Dayton, B.P. Fiske, W.J. Israelsen, K. R. Mattaini, N.I. Vokes, G. Stephanopoulos, L.C. Cantley, C.M. Metallo, J. W. Locasale, Metabolic pathway alterations that support cell proliferation, Cold Spring Harbor Symp. Quant. Biol. 76 (2011) 325–334, https://doi.org/10.1101/sqb.2012.76.010900.

[30] X. Li, X. Sun, P. Carmeliet, Hallmarks of endothelial cell metabolism in health and disease, Cell Metabol. 30 (2019) 414–433, https://doi.org/10.1016/j.cmet.2019.08.011.

[31] J. Hu, J.W. Locasale, J.H. Bielas, J. O'Sullivan, K. Sheahan, L.C. Cantley, M. G. Vander Heiden, D. Vitkup, Heterogeneity of tumor-induced gene expression changes in the human metabolic network, Nat. Biotechnol. 31 (2013) 522–529, https://doi.org/10.1038/nbt.2530.

[32] A. Schulze, A.L. Harris, How cancer metabolism is tuned for proliferation and vulnerable to disruption, Nature 491 (2012) 364–373, https://doi.org/10.1038/nature11706nature11706 [pii.

[33] X. Liu, J.W. Locasale, Metabolomics reveals intratumor heterogeneity – implications for precision medicine, EBioMedicine 19 (2017), https://doi.org/10.1016/j.ebiom.2017.04.030.

[34] D. Anastasiou, Tumour microenvironment factors shaping the cancer metabolism landscape, Br. J. Canc. 116 (2017) 277–286, https://doi.org/10.1038/bjc.2016.412.

[35] J.M. Brown, A.J. Giaccia, The unique physiology of solid tumors: opportunities (and problems) for cancer therapy, Canc. Res. 58 (1998) 1408–1416. http://www.ncbi.nlm.nih.gov/pubmed/9537241.

[36] D. Samanta, D.M. Gilkes, P. Chaturvedi, L. Xiang, G.L. Semenza, Hypoxia-inducible factors are required for chemotherapy resistance of breast cancer stem cells, Proc. Natl. Acad. Sci. U. S. A. 111 (2014) E5429–E5438, https://doi.org/10.1073/pnas.1421438111.

[37] A. McIntyre, A.L. Harris, Metabolic and hypoxic adaptation to anti-angiogenic therapy: a target for induced essentiality, EMBO Mol. Med. 7 (2015) 368–379, https://doi.org/10.15252/emmm.201404271.

[38] M. Curtarello, M. Tognon, C. Venturoli, M. Silic-Benussi, A. Grassi, M. Verza, S. Minuzzo, M. Pinazza, V. Brillo, G. Tosi, R. Ferrazza, G. Guella, E. Iorio, A. Godfroid, N.E. Sounni, A. Amadori, S. Indraccolo, Rewiring of lipid metabolism and storage in ovarian cancer cells after anti-VEGF therapy, Cells 8 (2019), https://doi.org/10.3390/cells8121601.

[39] Y. Cao, Adipocyte and lipid metabolism in cancer drug resistance, J. Clin. Invest. 129 (2019) 3006–3017, https://doi.org/10.1172/JCI127201.

[40] E. Currie, A. Schulze, R. Zechner, T.C. Walther, R. V Farese Jr., Cellular fatty acid metabolism and cancer, Cell Metabol. 18 (2013) 153–161, https://doi.org/10.1016/j.cmet.2013.05.017.

[41] S.A. Lim, J. Wei, T.L.M. Nguyen, H. Shi, W. Su, G. Palacios, Y. Dhungana, N. M. Chapman, L. Long, J. Saravia, P. Vogel, H. Chi, Lipid signalling enforces functional specialization of Treg cells in tumours, Nature 591 (2021), https://doi.org/10.1038/s41586-021-03235-6.

[42] J.A. Menendez, R. Lupu, Fatty acid synthase and the lipogenic phenotype in cancer pathogenesis, Nat. Rev. Canc. 7 (2007), https://doi.org/10.1038/nrc2222.

[43] S.F. Jones, J.R. Infante, Molecular pathways: fatty acid synthase, Clin. Canc. Res. 21 (2015) 5434–5438, https://doi.org/10.1158/1078-0432.CCR-15-0126.

[44] J. Yi, J. Zhu, J. Wu, C.B. Thompson, X. Jiang, Oncogenic activation of PI3K-AKT-mTOR signaling suppresses ferroptosis via SREBP-mediated lipogenesis, Proc. Natl. Acad. Sci. U.S.A. 117 (2020), https://doi.org/10.1073/pnas.2017152117.

[45] G.S. Hotamisligil, D.A. Bernlohr, Metabolic functions of FABPs–mechanisms and therapeutic implications, Nat. Rev. Endocrinol. 11 (2015) 592–605, https://doi.org/10.1038/nrendo.2015.122.

[46] H. Lee, F. Zandkarimi, Y. Zhang, J.K. Meena, J. Kim, L. Zhuang, S. Tyagi, L. Ma, T. F. Westbrook, G.R. Steinberg, D. Nakada, B.R. Stockwell, B. Gan, Energy-stress-mediated AMPK activation inhibits ferroptosis, Nat. Cell Biol. 22 (2020), https://doi.org/10.1038/s41556-020-0461-8.

[47] K.M. Gharpure, S. Pradeep, M. Sans, R. Rupaimoole, C. Ivan, S.Y. Wu, E. Bayraktar, A.S. Nagaraja, L.S. Mangala, X. Zhang, M. Haemmerle, W. Hu, C. Rodriguez-Aguayo, M. McGuire, C.S.L. Mak, X. Chen, M.A. Tran, A. Villar-Prados, G.A. Pena, R. Kondetimmanahalli, R. Nini, P. Koppula, P. Ram, J. Liu, G. Lopez-Berestein, K. Baggerly, S.E.L.A.K. Sood, FABP4 as a key determinant of metastatic potential of ovarian cancer, Nat. Commun. 9 (2018) 2923, https://doi.org/10.1038/s41467-018-04987-y.

[48] K.M. Nieman, H.A. Kenny, C. V Penicka, A. Ladanyi, R. Buell-Gutbrod, M. R. Zillhardt, I.L. Romero, M.S. Carey, G.B. Mills, G.S. Hotamisligil, S.D. Yamada, M. E. Peter, K. Gwin, E. Lengyel, Adipocytes promote ovarian cancer metastasis and provide energy for rapid tumor growth, Nat. Med. 17 (2011) 1498–1503, https://doi.org/10.1038/nm.2492.